The Astrophysical Journal, 775:99 (20pp), 2013 October 1 doi:10.1088/0004-637X/775/2/99

THE SPECTRALLY RESOLVED Lyα EMISSION OF THREE Lyα-SELECTED FIELD GALAXIES AT $z \sim 2.4$ FROM THE HETDEX PILOT SURVEY*

Taylor S. Chonis[1], Guillermo A. Blanc[2], Gary J. Hill[3], Joshua J. Adams[2], Steven L. Finkelstein[1], Karl Gebhardt[1], Juna A. Kollmeier[2], Robin Ciardullo[4,5], Niv Drory[3], Caryl Gronwall[4,5], Alex Hagen[4,5], Roderik A. Overzier[1,6], Mimi Song[1], and Gregory R. Zeimann[4,5]

[1] Department of Astronomy, University of Texas at Austin, 2515 Speedway, Stop C1400, Austin, TX 78712, USA; tschonis@astro.as.utexas.edu
[2] Observatories of the Carnegie Institution of Washington, 813 Santa Barbara Street, Pasadena, CA 91101, USA
[3] McDonald Observatory, University of Texas at Austin, 2515 Speedway, Stop C1402, Austin, TX 78712, USA
[4] Department of Astronomy & Astrophysics, The Pennsylvania State University, 525 Davey Lab, University Park, PA 16802, USA
[5] Institute for Gravitation and the Cosmos, The Pennsylvania State University, 104 Davey Lab #258, University Park, PA 16802, USA
[6] Observatório Nacional, Rua José Cristino 77, CEP 20921-400 São Cristóvão, Rio de Janeiro-RJ, Brazil
Received 2013 May 15; accepted 2013 August 5; published 2013 September 11

ABSTRACT

We present new results on the spectrally resolved Lyα emission of three Lyα-emitting field galaxies at $z \sim 2.4$ with high Lyα equivalent width (>100 Å) and Lyα luminosity ($\sim 10^{43}$ erg s^{-1}). At 120 km s^{-1} (FWHM) spectral resolution, the prominent double-peaked Lyα profile straddles the systemic velocity, where the velocity zero point is determined from spectroscopy of the galaxies' rest-frame optical nebular emission lines. The average velocity offset from systemic of the stronger redshifted emission component for our sample is 176 km s^{-1} while the average total separation between the redshifted and main blueshifted emission components is 380 km s^{-1}. These measurements are a factor of ∼2 smaller than for UV-continuum-selected galaxies that show Lyα in emission with lower Lyα equivalent widths. We compare our Lyα spectra to the predicted line profiles of a spherical "expanding shell" Lyα radiative transfer grid that models large-scale galaxy outflows. Specifically, blueward of the systemic velocity where two galaxies show a weak, highly blueshifted (by ∼1000 km s^{-1}) tertiary emission peak, the model line profiles are a relatively poor representation of the observed spectra. Since the neutral gas column density has a dominant influence over the shape of the Lyα line profile, we caution against equating the observed Lyα velocity offset with a physical outflow velocity, especially at lower spectral resolution where the unresolved Lyα velocity offset is a convoluted function of several degenerate parameters. Referring to rest-frame ultraviolet and optical *Hubble Space Telescope* imaging, we find that galaxy–galaxy interactions may play an important role in inducing a starburst that results in copious Lyα emission as well as perturbing the gas distribution and velocity field, both of which have strong influence over the Lyα emission line profile.

Key words: galaxies: evolution – galaxies: high-redshift – galaxies: ISM – galaxies: starburst – line: profiles – radiative transfer

Online-only material: color figures

1. INTRODUCTION

As the strongest spectral feature of the most abundant element in the universe, the Lyα transition of hydrogen ($n = 2 \rightarrow 1$; 1216 Å) has become one of the most widely utilized tools for detecting galaxies in the early universe (e.g., Hu & McMahon 1996; Cowie & Hu 1998; Rhoads et al. 2000; Steidel et al. 2000; van Breukelen et al. 2005; Gronwall et al. 2007; Finkelstein et al. 2009; Rauch et al. 2011; Adams et al. 2011). Lyα is versatile in that it can probe the extremes of the high-redshift galaxy census, such as faint, low-mass populations (e.g., Rauch et al. 2008) and the high-energy systems at the top end of the mass function (e.g., Willott et al. 2011).

Lyα photons are produced as a result of excitation or ionization of neutral hydrogen and can arise in a variety of astrophysical scenarios relating to high-redshift galaxies. These include cooling radiation as a result of gravitational collapse (e.g., Faucher-Giguére et al. 2010) or extremely rapid gas motions (i.e., shocks; Birnboim & Dekel 2003), photoionization by stars (e.g., Partridge & Peebles 1967) or an active galactic nucleus (AGN; e.g., Haiman & Rees 2001), or fluorescence of neutral gas in the intergalactic medium (IGM; e.g., Kollmeier et al. 2010). However, the interpretation of the emergent Lyα spectra is non-trivial due to the resonant nature of the transition in neutral hydrogen, in which the line is optically thick for even small neutral fractions (Gunn & Peterson 1965). This property makes the escape of Lyα photons from a galaxy a complex radiative process that is highly dependent on the properties of the interstellar medium (ISM) and surrounding circumgalactic medium, such as gas kinematics, covering fraction, geometry, and dust content. The result of Lyα radiative transfer through the ISM is a significant modulation of the intrinsic Lyα emission line profile, both spatially and spectrally. The emergent emission line profile can be further modified by transfer through the surrounding IGM, which can absorb a significant amount of radiation in the vicinity and blueward of Lyα (e.g., Laursen et al. 2011). Because of the amount of physics that can be encoded within the emergent Lyα line profile, a great deal of theoretical work has gone into understanding Lyα radiative transfer to aid in the interpretation of observed Lyα spectra of galaxies. In particular, the use of Monte Carlo numerical techniques has become standard practice (e.g., Lee 1974; Ahn et al. 2000; Zheng & Miralda-Escudé 2002; Tasitsiomi 2006; Hansen & Oh 2006; Dijkstra et al. 2006a; Verhamme et al. 2006), and has provided useful predictions of the emergent Lyα line profile for

* This paper includes data taken at The McDonald Observatory of The University of Texas at Austin.

comparison with observations for a variety of different physical scenarios. The implementation of such radiative transfer codes are currently being advanced by post-processing more realistic models of galaxies drawn from hydrodynamic and cosmological simulations (e.g., Zheng et al. 2010; Kollmeier et al. 2010; Barnes et al. 2011; Verhamme et al. 2012; Yajima et al. 2013).

Non-active galaxies that are selected by virtue of their Lyα emission with an equivalent width $EW_{Ly\alpha} > 20$ Å (i.e., Lyα emitters, LAEs) are typically low mass ($\lesssim 10^{9.5}\ M_\odot$) with young stellar populations ($\lesssim$100 Myr) and are forming stars at rates of $\lesssim 10\ M_\odot\ yr^{-1}$ (e.g., Venemans et al. 2005; Gawiser et al. 2006; Finkelstein et al. 2007; Ono et al. 2010; Acquaviva et al. 2011). In addition, some LAEs appear to have non-negligible dust content (Finkelstein et al. 2009; Pentericci et al. 2009), low gas-phase metallicity (Finkelstein et al. 2011; Nakajima et al. 2013), and compact, irregular spatial morphologies (e.g., Venemans et al. 2005; Gronwall et al. 2011; Bond et al. 2012). At least some of these properties appear to not evolve significantly with redshift (e.g., Ouchi et al. 2008; Blanc et al. 2011; Mallery et al. 2012). A significant fraction of ultraviolet (UV) continuum-selected galaxies (i.e., Lyman break galaxies, LBGs) also show Lyα in emission (e.g., Shapley et al. 2003; Kornei et al. 2010; Stark et al. 2010; Kulas et al. 2012; Ono et al. 2012; Berry et al. 2012). LBGs typically have lower $EW_{Ly\alpha}$ (some show Lyα in absorption), more evolved stellar populations, and are more massive than the typical Lyα-selected galaxy (e.g., Gawiser et al. 2006; Pentericci et al. 2007; Yuma et al. 2010).

In a star-forming galaxy, Lyα photons are produced from recombinations in hydrogen gas that was ionized by the UV radiation of massive, main sequence stars in H II regions. Unlike UV continuum or photons from other optically thin transitions that hail from the same H II region (e.g., Hα), Lyα photons become resonantly trapped in the first parcels of neutral hydrogen they encounter. As compared to the optically thin photons, the path length of Lyα to escape the galaxy is increased due to the scattering, making it especially sensitive to dust absorption. The path length of Lyα photons through neutral hydrogen can be further altered by local velocity fields due to thermal motion, turbulence, and bulk motions (e.g., due to supernovae or stellar driven winds, or by galaxy–galaxy interactions), thereby shifting Lyα photons in and out of resonance and affecting the emergent line profile (e.g., Verhamme et al. 2006). This potentially makes the emergent Lyα spectrum a very powerful probe of gas kinematics (e.g., Verhamme et al. 2008; Yang et al. 2011; Kulas et al. 2012), especially when the spectrum can be spatially resolved (e.g., Rauch et al. 2011).

Evidence for large-scale outflows is wide-spread in high-redshift star-forming galaxies (e.g., Shapley et al. 2003; Martin 2005; Berry et al. 2012). In LBGs, for example, the galaxy's redshift differs when measured from the interstellar (IS) absorption lines versus the Lyα emission line (by $\gtrsim$600 km s^{-1}), which implies that one or both features are not at rest with respect to the stars in the galaxy (Shapley et al. 2003). Systemic redshifts and gravitationally induced motion are expected to be well represented by nebular emission lines such as Hα, which is optically thin and whose strength depends upon the UV radiation field in the same vicinity as the origin of the Lyα photons (Erb et al. 2006). In LBGs, the IS absorption lines are blueshifted with respect to the Hα-based systemic redshift (by $\sim$160 km s^{-1}) while the peak of the Lyα emission line is typically redshifted (by $\sim$450 km s^{-1}; Steidel et al. 2010). Although the interpretation of the redshifted Lyα emission is non-trivial due to the transition's resonant scattering nature, the blueshifted IS absorption is a strong indicator of a galactic outflow and is caused by the absorption of stellar light in swept-up material that is approaching along the observer's line of sight.

Recently, observations of rest-frame optical nebular emission lines (e.g., Hβ, [O III], or Hα, depending on the redshift of the galaxy) for $2 \lesssim z \lesssim 3$ LAEs observed in the near-infrared (NIR) have become more common. These data provide not only standard rest-frame optical emission line diagnostics for these high-redshift galaxies (e.g., Finkelstein et al. 2011; Song et al. 2013; M. Song et al. 2013, in preparation), but also a measure of their systemic redshifts (McLinden et al. 2011; Hashimoto et al. 2013; Guaita et al. 2013). Thus, Lyα velocity offsets are now be measured for LAEs much in the same way as for LBGs (e.g., Steidel et al. 2010; Kulas et al. 2012), which provides an additional constraint when comparing Lyα radiative transfer models to the observed Lyα spectra of LAEs. However, velocity offsets of Lyα alone cannot necessarily constrain the gas kinematics and may not correlate directly with bulk gas velocities. Useful kinematic information can be encoded within the offset Lyα line profile in the form of asymmetries and other finer-scale spectral features, such as multiple emission peaks. This information can potentially be lost when observed at low spectral resolution, as has been used in multiple studies that probe Lyα velocity offsets (e.g., Finkelstein et al. 2011; McLinden et al. 2011; Kulas et al. 2012; Guaita et al. 2013; M. Song et al. 2013, in preparation). Multiple peaks are a natural consequence of Lyα resonant line transfer (e.g., Neufeld 1990), and the frequency of multiple-peaked Lyα spectra in LAE and LBG samples has recently been studied by Yamada et al. (2012) and Kulas et al. (2012), respectively. Both studies find that multiple-peaked Lyα line profiles comprise $\gtrsim$50% of their respective samples, which should be regarded as lower limits due to the limited S/N and spectral resolution of the Lyα data.

Combined with the recent observational evidence that shows that LAEs have smaller Lyα velocity offsets as compared to LBGs (Hashimoto et al. 2013), the spectral substructure that studies such as Yamada et al. (2012) and Kulas et al. (2012) have uncovered motivates observations of Lyα at higher spectral resolution. Such observations will probe the ISM and circumgalactic medium through which the Lyα photons traverse, and provide more stringent constraints on existing Lyα radiative transfer models. In this paper, we present new higher resolution (120 km s^{-1} FWHM) optical spectra of the Lyα emission of three galaxies that were initially discovered in the HETDEX Pilot Survey (HPS; Adams et al. 2011). We discuss these data in Section 2. In Section 3, we present basic observational results from our optical spectroscopy and compare the three Lyα emission line profiles with those of other Lyα and UV-continuum-selected samples. In Section 4, we present a quantitative comparison of the observed Lyα line profiles with the predictions of existing Lyα radiative transfer models with a spherical expanding shell gas geometry. In Section 5, we discuss our findings and finally present our conclusions in Section 6.

Throughout this paper, we assume a flat ΛCDM cosmology ($H_0 = 70$ km s^{-1} Mpc^{-1}, $\Omega_m = 0.27$, $\Omega_\Lambda = 0.73$; Komatsu et al. 2011). For the atomic transitions discussed, we use the following vacuum wavelengths in Å quoted from the Atomic Line List v2.04[7]: Lyα (1215.670), [O III] λ5007 (5008.240), and Hα (6564.610). All magnitudes are reported in the AB system (Oke & Gunn 1983).

[7] Atomic Line List v2.04: http://www.pa.uky.edu/~peter/atomic/

Table 1
Observed Properties of Targeted HETDEX Pilot Survey Galaxies

Property	Units	HPS194	HPS256	HPS251	Source[a]
R.A.	J2000	10:00:14.18	10:00:28.33	10:00:27.23	A11[b]
Decl.	(J2000)	+02:14:26.11	+02:17:58.44	+02:17:31.50	
$z_{Ly\alpha}$	...	2.2896 ± 0.0004	2.4923 ± 0.0004	2.2865 ± 0.0004	A11[c]
z_{sys}	...	2.28628 ± 0.00002	2.49024 ± 0.00004	2.28490 ± 0.00005	F11[d], S13[d]
$\Delta v_{Ly\alpha}$	km s^{-1}	303 ± 28	177^{+52}_{-68}	146^{+116}_{-156}	A11[c], F11[d], S13[d]
$F_{Ly\alpha}$	10^{-17} erg s^{-1} cm^{-2}	$61.0^{+4.9}_{-4.3}$	$31.4^{+9.3}_{-6.5}$	$45.0^{+13.7}_{-11.6}$	A11
$L_{Ly\alpha}$	10^{42} erg s^{-1}	25.1 ± 1.9	16.4 ± 4.1	18.5 ± 5.2	
$EW_{Ly\alpha}$	Å	114 ± 13	206 ± 65	140 ± 43	B11
$\sigma_{H\alpha}$	km s^{-1}	61 ± 9	72 ± 9	44 ± 6	F11, S13
V	mag	24.07 ± 0.05	25.07 ± 0.09	24.70 ± 0.07	COSMOS[e]
$E(B-V)$	mag	0.09 ± 0.06	0.10 ± 0.09	0.07 ± 0.08	B11
SFR(Hα)	$M_\odot$ yr^{-1}	>29.3	>35.4	>9.9	F11, S13[f]
$12 + \log(O/H)$	...	<7.87	<8.12	<8.00	F11, S13[g]
Stellar mass	$10^8\ M_\odot$	155^{+31}_{-43}	$1.9^{+0}_{-0.1}$	11^{+2}_{-1}	F11, S13

Notes.
[a] A11: Adams et al. (2011); F11: Finkelstein et al. (2011); S13: M. Song et al. (2013, in preparation); B11: Blanc et al. (2011).
[b] The equatorial coordinates correspond to the optical counterpart to the Lyα emission.
[c] Given for the HPS $R \approx 750$ Lyα spectra after the correction for V_{LSR} and for the n_{atm} error (see Section 3.1). The Lyα velocity offset is calculated from these data as $\Delta v_{Ly\alpha} = c\,(z_{Ly\alpha} - z_{sys}) / (z_{sys} + 1)$. The quoted uncertainties are statistical. Systematic errors associated with the wavelength calibration are discussed in Section 3.1.
[d] Given for the NIRSPEC data after recalculation using the proper vacuum wavelengths for [O III] and Hα (see Section 2.3.1). For HSP251, z_{sys} is determined from Hα only. The quoted uncertainties are statistical. Systematic errors associated with the wavelength calibration are discussed in Section 2.3.1.
[e] COSMOS Intermediate and Broad Band Photometry Catalog, 2009 April Release. The magnitudes have been corrected to total using the supplied band-independent aperture corrections. Also see Ilbert et al. (2009).
[f] Given from the measured Hα line fluxes *without a dust correction* and assuming the star formation scaling relation of Kennicutt (1998).
[g] The oxygen abundances are given as 1σ upper limits.

2. OBSERVATIONS AND DATA REDUCTION

2.1. Sample Selection—The HETDEX Pilot Survey

The Hobby–Eberly Telescope Dark Energy Experiment (HETDEX; Hill et al. 2008a) will use 0.8 million LAEs as tracers of the galaxy power spectrum and measure the evolution of dark energy from $1.9 < z < 3.5$ with high precision. This ~420 deg^2 (~9 Gpc^3) blind spectroscopic survey will be conducted with the Hobby–Eberly Telescope and a revolutionary new multiplexed instrument called the Visible Integral-field Replicable Unit Spectrograph (VIRUS; Hill et al. 2012). As a test-bed for HETDEX, a single prototype VIRUS unit integral field spectrograph (the Mitchell Spectrograph; formerly known as VIRUS-P; Hill et al. 2008b) has resided at the McDonald Observatory's Harlan J. Smith 2.7 m telescope since 2007 and has conducted a ~100 night, ~169 arcmin^2 (~10^6 Mpc^3) pilot survey for HETDEX in which 99 star-forming (i.e., non-AGN) LAEs were discovered at redshifts $2 < z < 4$. The survey design, catalog, and initial science results can be found in Adams et al. (2011) and Blanc et al. (2011).

As described in Section 1, observations of the rest-frame optical nebular emission lines are especially important for constraining models of Lyα radiative transfer and gas kinematics in star-forming galaxies. Given the aforementioned focus of this paper, we require prior knowledge of the galaxy systemic redshift as measured from the rest-frame optical nebular emission lines. For two HPS LAEs (catalog IDs 194 and 256), these data have been published in Finkelstein et al. (2011). Additionally, the only existing optical spectra previous to this work for these galaxies are from the HPS in which the Mitchell Spectrograph observed with 5.5 Å resolution (~400 km s^{-1} FWHM at 4100 Å), yielding unresolved Lyα emission lines (Adams et al. 2011). Given the existing data available for these two galaxies, we have chosen to conduct follow-up observations with higher resolution optical spectroscopy. For convenience, some relevant properties of HPS194 and HPS256 are tabulated from the current HPS publications in Table 1. The only preselection for the galaxies in this follow-up study is that they have an Lyα flux $F_{Ly\alpha} \gtrsim 10^{-16}$ erg s^{-1} cm^{-2} to ease the detection of the rest-frame optical lines (note that 86 of the 99 non-AGN HPS LAEs meet such a selection criteria). Additionally, note that the galaxies included in this study are bright enough in the continuum to be considered LBGs in most surveys (e.g., Steidel et al. 2004).

2.2. Mitchell Spectrograph Optical Spectroscopy

We obtained follow-up optical spectra of the Lyα emission of HPS194 and HPS256 using the Mitchell Spectrograph (Hill et al. 2008b) on the Harlan J. Smith 2.7 m telescope at the McDonald Observatory on the nights of UT 2010 February 13 and 14, respectively. In an attempt to spectrally resolve the Lyα feature of these galaxies, we replaced the 831 line mm^{-1} grating that was used to carry out the HPS with a 2400 line mm^{-1} grating. This grating yields a spectral resolution of $\Delta\lambda = 1.6$ Å (120 km s^{-1} FWHM at 4100 Å) over the wavelength range $3690 < \lambda$ (Å) < 4400 ($R = \lambda/\Delta\lambda \approx 2500$).

The Mitchell Spectrograph is an integral field spectrograph that has high throughput for blue wavelengths (~40% at 4100 Å; Hill et al. 2008b). The $107'' \times 107''$ square field of view integral field unit (IFU) contains 246 fibers arranged in a hexagonal close pack pattern with one-third fill factor. Each fiber has a diameter of $4\farcs24$ on the sky (~36 kpc at $z \sim 2.4$). For these observations, we position a single fiber on the coordinates of each targeted galaxy that correspond to the most likely optical

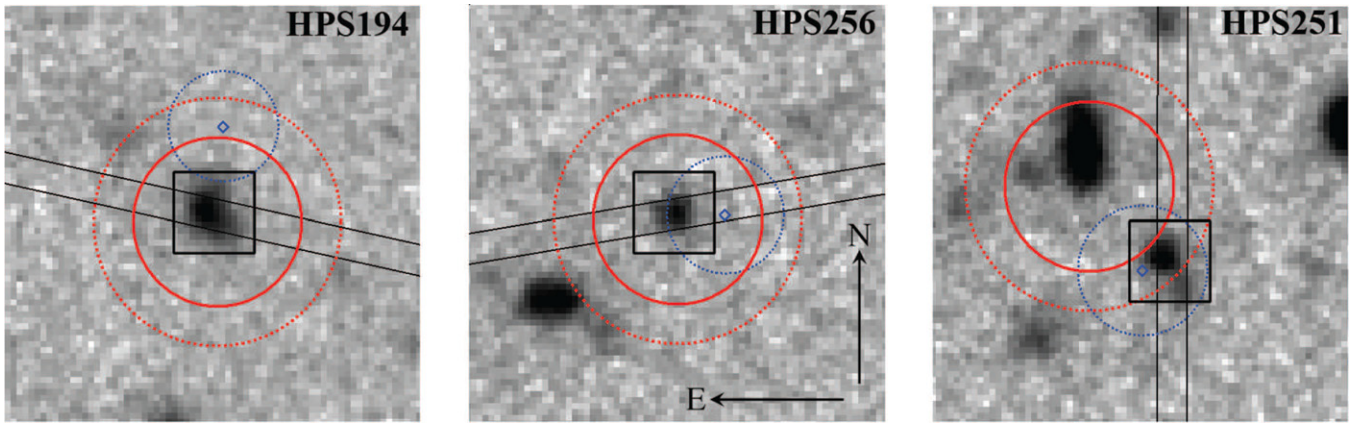

Figure 1. Subaru *V*-band images (10.″5 × 10.″5 in size) showing the field surrounding each targeted galaxy. The solid red circle indicates the position of the 4.″24 diameter Mitchell Spectrograph fiber while the concentric dashed circle indicates the extent of the rms uncertainty in its position on the sky. The blue diamond and the surrounding dashed blue circle indicate the Lyα centroid and positional error, respectively, from the HPS (Adams et al. 2011). The black lines indicate the width and position angle of the NIRSPEC slit used by Finkelstein et al. (2011) for HPS194 and HPS256 and by M. Song et al. (2013, in preparation) for HPS251. The 2.″5 × 2.″5 box is centered on the coordinates of the most likely continuum counterpart to the Lyα emission (Adams et al. 2011) and shows the spatial extent of the *HST* images discussed in Section 5.5.

(A color version of this figure is available in the online journal.)

continuum counterpart to the detected Lyα emission, as determined by Adams et al. (2011). For the HPS256 pointing, the IFU was positioned such that another nearby HPS LAE (catalog ID 251) fell within the field of view and near the edge of another fiber. Note that HPS194, HPS256, and HPS251 are unresolved within the fiber in the $\lesssim$2″ FWHM seeing during our observations. The remaining fibers in the IFU sample the sky to provide excellent sky subtraction. The astrometry of the individual fiber positions was calibrated to 1.″0 rms. In Figure 1, we show Subaru *V*-band images (Taniguchi et al. 2007) from the Cosmic Evolution Survey (COSMOS; Scoville et al. 2007; see also Section 2.3.2) in which we indicate the fiber positions relative to the continuum counterparts and the centroid of the Lyα emission (as determined by Adams et al. 2011).

The data were taken with 2 × 1 CCD binning in the spectral direction. This results in a dispersion of 0.69 Å per binned pixel (i.e., there are 2.3 binned pixels per resolution element along the spectral direction). The read noise of the CCD is 3.8 e^- which allows for sky noise dominated spectra in the 1800 s integration times used throughout the observing run. The CCD gain was set to 1.0 e^- ADU^{-1}. For both the HPS194 and the HPS256 pointings, we obtained six hours of total integration in dark and clear conditions. All science exposures were acquired at an airmass of <1.2. Two flux standard stars were observed each night to correct for the instrumental response.

The data were reduced with the custom pipeline VACCINE (Adams et al. 2011). VACCINE carries out standard reduction procedures for overscan and bias correction. Twilight flats, which were taken both at dawn and dusk each night, are combined and used to locate and trace each of the 246 spectra on the CCD. To properly correct the pixel-to-pixel variations, fiber-to-fiber relative transmission, and the fiber spatial profile, the solar spectrum must be removed from the twilight flats which requires a wavelength solution. Unfortunately, the suite of calibration lamps available did not yield enough comparison lines for determining a reliable wavelength solution for our instrumental setup. Therefore, we extracted a wavelength solution from the twilight flats themselves by convolving a template solar spectrum (Kurucz et al. 1984) to the instrumental resolution and fitting the result to the combined twilight flats. The fit for each fiber is parameterized as a polynomial of the fourth degree as a function of pixel, where the second-order terms are constrained across the fibers to be a smooth function for greater solution stability. An independent wavelength solution results for each fiber on each night. From the rms in the residuals of the fitted solar features, we expect this wavelength solution to be accurate to ∼0.1 Å (∼7 km s^{-1} for Lyα at $z \sim 2.4$). By measuring the centroids of solar absorption features in the dusk and dawn twilight flats separately (which were taken at the high and low temperatures recorded each night, respectively), we find that this wavelength solution systematically drifts with changing thermal conditions by <0.15 Å (<11 km s^{-1} for Lyα at $z \sim 2.4$). Once the spectra for a given night are combined (see below), this systematic error results in a negligible degradation of the spectral resolution of the final reduced spectrum. After correcting the combined twilight flat for the solar spectrum and normalizing, the science data are extracted and flat-fielded. The combined sky spectrum from the empty fibers is fit with a B-spline and subtracted from the fiber containing the target galaxy (Dierckx 1993; Kelson 2003). Finally, cosmic rays are masked. The resulting individual science spectra are collapsed along the fiber spatial direction by a weighted mean ignoring the pixels that were masked for cosmic rays, where the weights are determined from the Poisson and Gaussian uncertainties due to photon counting and read noise, respectively.

Each one-dimensional (1D) science spectrum is further corrected for atmospheric extinction using a model specific to McDonald Observatory as well as for the instrumental response using the co-added flux standard star spectra. The individual corrected 1D science spectra for each galaxy are then combined by a weighted, $\pm 3\sigma$-clipped mean, where the weight for each spectrum is determined from differential photometry of stars that were congruently observed with the science exposures by the Mitchell Spectrograph's CCD guider. Due to the stability of the instrument (see the previous paragraph), a single wavelength solution applies for a given fiber throughout the entire night and no resampling of the science spectra are required before combination. Upon examination of the combined spectra for each galaxy (including HPS251), we find that we have made detections of the Lyα feature in which multiple emission components are visible at S/N $\gtrsim$ 3. Using an assumed wavelength-independent index of refraction for air at the altitude of McDonald Observatory

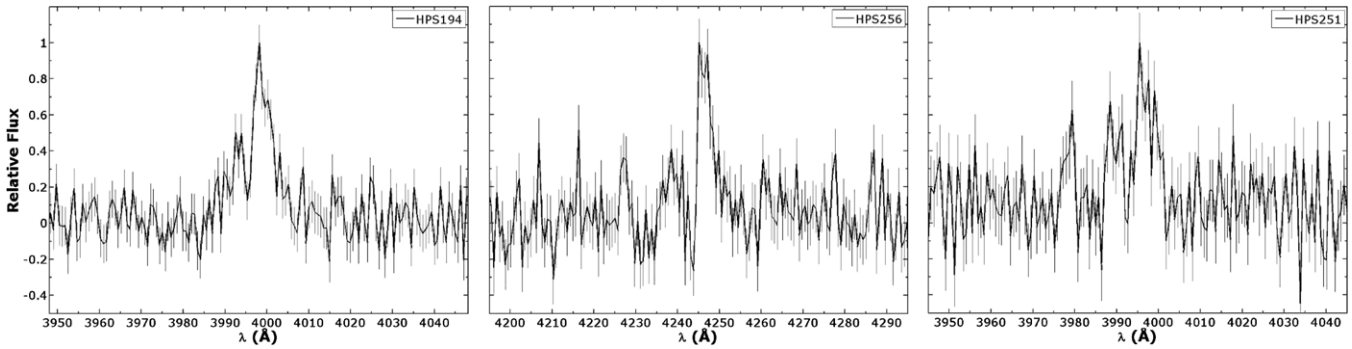

Figure 2. Mitchell Spectrograph optical spectra of the targeted galaxies plotted against the observed wavelength at $R \approx 2500$. The spectra show a ± 50 Å window, centered on the detected Lyα feature. Each spectrum has been normalized to the peak flux observed in the line. The error bars indicate the 1σ statistical uncertainties at each wavelength, which are typically ± 0.11 for HPS194, ± 0.14 for HPS256, and ± 0.17 for HPS251 in the relative flux units displayed.

($n_{\rm atm} = 1.00022$), each combined 1D spectrum is shifted into vacuum conditions. Finally, for proper comparison with the rest-frame optical nebular emission lines (see Section 2.3.1), we further correct the wavelength scale for the relative motion of the Earth with respect to the local standard of rest at the time of observation using the $V_{\rm LSR}$ calculator.[8] In Figure 2, we show a ± 50 Å subsection of the final 1D spectra, centered on Lyα. Since we have successfully detected the Lyα emission from HPS251 despite it not being a primary target, we include a compilation of its observed properties in Table 1 along with HPS194 and HPS256.

2.3. Ancillary Data

2.3.1. NIRSPEC Rest-frame Optical Spectroscopy

The interpretation of our Lyα spectra relies on knowing the galaxies' systemic redshifts $z_{\rm sys}$. The data required for making this measurement were taken at the 10 m Keck II telescope with the NIRSPEC instrument (McLean et al. 1998), as presented by Finkelstein et al. (2011) for HPS194 and HPS256 and M. Song et al. (2013, in preparation) for HPS251 (also, see Song et al. 2013). These authors have detected at least one rest-frame optical nebular emission line for each galaxy at $>3\sigma$ significance (Hα for all three galaxies in addition to [O III] λ5007 for HPS194 and HPS256) and used the observed wavelengths to calculate $z_{\rm sys}$. However, Finkelstein et al. (2011) did not use the vacuum wavelengths of the [O III] λ5007 and Hα transitions when comparing to the corresponding observed wavelengths (which *were* corrected into a vacuum frame and to the local standard of rest). M. Song et al. (2013, in preparation) have performed a new and improved reduction of the Finkelstein et al. (2011) HPS194 and HPS256 data and have recalculated the [O III] λ5007 and Hα-based redshifts using the vacuum wavelengths listed in Section 1. The newly calculated weighted average values of $z_{\rm sys}$ for these galaxies are listed in Table 1 along with each measurement's statistical uncertainty. The 1D Hα emission line profile for each galaxy can be seen in lower panels of Figure 3.

As described by Finkelstein et al. (2011), small errors in the wavelength solutions of the *H*- and *K*-band NIRSPEC data (i.e., the instrumental setups for detecting [O III] λ5007 and Hα, respectively) result in slightly different values of $z_{\rm sys}$ for a given galaxy depending on which emission line is being measured. As a result, Finkelstein et al. (2011) assigned an additional systematic error term to $z_{\rm sys}$. After the new reduction by M. Song et al. (2013, in preparation), the $z_{\rm sys}$ systematic error for HPS194 and HPS256 has been improved to ± 0.00013 and ± 0.00014, respectively ($\sim$12 km s^{-1} at $z \sim 2.4$). Note that the systematic error cannot be calculated for HPS251 as described by Finkelstein et al. (2011) since Hα was the only line used to determine its $z_{\rm sys}$. To be conservative in our analysis, we will assume that the larger systematic error associated with the HPS256 $z_{\rm sys}$ measurement also applies for HPS251.

2.3.2. COSMOS and CANDELS Public Data

All three galaxies reside within the COSMOS[9] survey (Scoville et al. 2007) and Cosmic Assembly Near-infrared Deep Extragalactic Legacy Survey (CANDELS; Grogin et al. 2011) footprints. When necessary in this work, we utilize the wealth of publicly available data from these surveys and note the relevant catalog(s) and citation(s). In particular, we will utilize the CANDELS version 1.0 *Hubble Space Telescope* (*HST*) Advanced Camera for Surveys (ACS) Wide Field Channel (WFC) F606W images and Wide Field Camera 3 (WFC3)/Infrared (IR) channel F160W images to consider the spatial morphologies and distribution of sources around the galaxies (Koekemoer et al. 2011). The former probes the three galaxies in the rest-frame UV at $\sim$1800 Å while the latter does so in the rest-frame optical at $\sim$4700 Å.

3. OBSERVATIONAL RESULTS

3.1. Lyα Velocity Offsets from the HETDEX Pilot Survey

Finkelstein et al. (2011) determined the Lyα velocity offset from the systemic line center $\Delta v_{\rm Ly\alpha}$ by comparing the redshifts as determined from the rest-frame optical lines ($z_{\rm sys}$) and that for Lyα ($z_{\rm Ly\alpha}$). They originally found $\Delta v_{\rm Ly\alpha} = 162 \pm 37 \pm 42$ km s^{-1} and $36 \pm 35 \pm 18$ km s^{-1} for HPS194 and HPS256, respectively. The first set of quoted uncertainties are statistical and display the uncertainty in locating the centroid of a low S/N emission line while the second set are systematic resulting from the differences in the wavelength solutions of the *H*- and *K*-band NIRSPEC data (see Finkelstein et al. 2011 for details). The systematic error resulting from the wavelength calibration of the HPS data is insignificant compared to these error terms (Adams et al. 2011). Given the corrected $z_{\rm sys}$ values discussed in Section 2.3.1, these velocity offsets are actually larger than what was originally calculated by Finkelstein et al. (2011).

[8] $V_{\rm LSR}$ Calculator, based on chapter 6.1 of Meeks (1976): http://www.astro.virginia.edu/emm8x/utils/vlsr.html

[9] COSMOS Archive—Released Datasets: http://irsa.ipac.caltech.edu/data/COSMOS/datasets.html

During the reduction of our $R \approx 2500$ Lyα spectra, we compared the central Lyα wavelength to that quoted for each respective object in the HPS catalog (Adams et al. 2011). Through this comparison, we discovered that the central wavelengths quoted in Table 3 of that work are actually in error, which was caused by a division of the observed wavelengths by the atmospheric index of refraction $n_{\rm atm}$ (rather than a multiplication) when correcting to vacuum conditions. To recover the central Lyα wavelengths with a proper correction into vacuum conditions, one can multiply the values of Column 4 in that table by ${n_{\rm atm}}^2 = (1.00022)^2$. This corresponds to a 0.9 Å (65 km s^{-1}) increase in the original quoted central wavelengths for Lyα at $z \sim 2.4$. With the new corrected values of $z_{\rm sys}$, applying this additional correction as well as a $V_{\rm LSR}$ correction to the HPS optical data of Adams et al. (2011) results in new velocity offsets of $\Delta v_{\rm Ly\alpha} = 303$ km s^{-1} and 177 km s^{-1} for HPS194 and HPS256, respectively. In addition, we reevaluate the statistical uncertainty in the velocity centroids by fitting a Gaussian to 10^3 Monte Carlo realizations of the observed HPS spectrum, where the flux in each realization was varied according to the derived 1σ statistical errors (assuming they are normally distributed). The uncertainties encompass the 68% confidence interval, and are ± 28 km s^{-1} for HPS194 and $^{+52}_{-68}$ km s^{-1} for HPS256. We apply the same corrections and uncertainty estimation methods to the HPS Lyα data for HPS251; using the NIR results of M. Song et al. (2013, in preparation), we calculate $\Delta v_{\rm Ly\alpha} = 146^{+116}_{-156}$ km s^{-1}. These results are tabulated in Table 1.

In the top panels of Figure 3, we show the co-added $R \approx 750$ HPS spectra (using data from all HPS fibers in which Lyα was detected). Two of the three galaxies are shown to have statistically significant velocity offsets, which may suggest the presence of large-scale outflows in their ISM. It will be seen when examining the higher resolution $R \approx 2500$ spectra that the bulk offset of the unresolved emission lines at low spectral resolution are difficult to interpret due to the complicated Lyα radiative transfer in these galaxies.

3.2. Characterization of the $R \approx 2500$ Lyα Spectra

3.2.1. Multiple-peaked Lyα Emission Line Profiles

In the lower panels of Figure 3, we use $z_{\rm sys}$ for each galaxy to convert the wavelength scale of the $R \approx 2500$ spectra into velocity space, where $\Delta v = 0$ km s^{-1} corresponds to the Hα line center. Each galaxy appears to display a complex Lyα line profile with at least two emission components straddling the velocity zero point with absorption (i.e., lack of emission) at the Lyα line center. In all cases, the strongest emission component lies redward of the velocity zero point and appears quite asymmetric with an extended redward tail. Additionally, each galaxy shows significant emission blueward of the Lyα line center. HPS194 shows a single, relatively weak blueward emission peak. HPS256 and HPS251 show a similar weak blue peak as HPS194 *in addition to* second blueshifted peaks located at approximately -1000 km s^{-1} for each galaxy with S/N = 2.8 and 3.0, respectively.

Recent results have shown that multiple-peaked Lyα emission line profiles are common among star-forming galaxies (e.g., Kulas et al. 2012; Yamada et al. 2012), especially the "characteristic" double-peaked profile having a stronger red peak with an accompanying weaker blue emission component straddling the velocity zero point. The Lyα line profile of HPS194 easily fits this description. Kulas et al. (2012) find that such profiles ("Group 1" in their nomenclature) consist of 61% of their sample of 18 $z \sim 2$–3 Lyα-emitting LBGs that were preselected to have multiple Lyα peaks with measures of $z_{\rm sys}$ from observations of Hα or [O III] in the NIR. Additionally, while Yamada et al. (2012) have no measure of $z_{\rm sys}$ for their large sample of 91 $z \sim 3.1$ LAEs in the SSA22-Sb1 field without a multiple-peaked preselection, they do find that $\geqslant$44% of their measured Lyα spectra appear "Group 1"-like in having two emission components where the redder component is stronger. We present further discussion and more examples of double-peaked Lyα line profiles from the literature in Section 3.3.

Excluding the highly blueshifted emission components at -1000 km s^{-1} in the HPS256 and HPS251 Lyα spectra, these two galaxies also appear to fit the "Group 1" Lyα line profile morphology. As such, we look further into the nature of the bluest peak for each of these two galaxies. The peaks under scrutiny are marked in Figure 3 by the light-blue shaded regions, which have been centered on the central velocity of the peak as determined through a Gaussian fit to the emission component in the $R \approx 2500$ data. The width of the shaded region corresponds to one spectral resolution element of the $R \approx 750$ data. Since the velocity offset of this emission peak is so large, it should be cleanly resolved in the HPS $R \approx 750$ spectra. However, we see no evidence of emission beyond the 1σ statistical uncertainties at the corresponding velocity in the $R \approx 750$ data for either HPS256 or HPS251. Note that this does not rule out the reality of these features in the $R \approx 2500$ spectra. In the top panels of Figure 3, we also show the $R \approx 2500$ data convolved to the spectral resolution and interpolated to the dispersion of the HPS. As can be seen, the lower spectral resolution smears out the weak emission peak to within the 1σ statistical uncertainties for both galaxies, so we do not expect to clearly detect them in the HPS spectra.

We have examined the possibility that the low S/N second blueward peaks are the result of systematic or random effects in the $R \approx 2500$ data. Despite that HPS256 and HPS251 were observed in the same field, the two galaxies have different $z_{\rm sys}$. Thus, the second blueshifted peaks do not correspond to the same observed wavelength even though they have very similar velocity offsets relative to the systemic redshift. We have examined the extracted sky spectra from the fibers in the IFU that are adjacent to those containing the LAEs to look for sky absorption or emission features in the vicinity of the second blueward peaks. We find none for HPS251. For HPS256, the second blueward emission peak lies within one spectral resolution element of a sky absorption feature. However, we find no evidence of a systematic sky subtraction error since we do not see peaks with similar S/N in the reduced spectra of adjacent fibers at the wavelength corresponding to that of the second blueward emission peak. Additionally, we have visually examined the two-dimensional (2D) spectra of the fibers containing the LAEs in each individual CCD exposure after the cosmic ray masking procedure to verify that no cosmic rays or other artifacts were left unmasked in the vicinity of the Lyα spectra. Finally, we experimented with our data combination rejection procedure by recomputing the $\pm 3\sigma$-clipped weighted mean on the 2D data before collapsing to the final 1D spectra. Performing the combination with the increased pixels space should yield a more robust rejection of outlying pixel values. After collapsing this combined 2D spectra along the fiber spatial direction, we find that the resulting reduced Lyα line profiles are statistically identical to those in the original data reduction described in Section 2.2 and that the second blueward peaks are

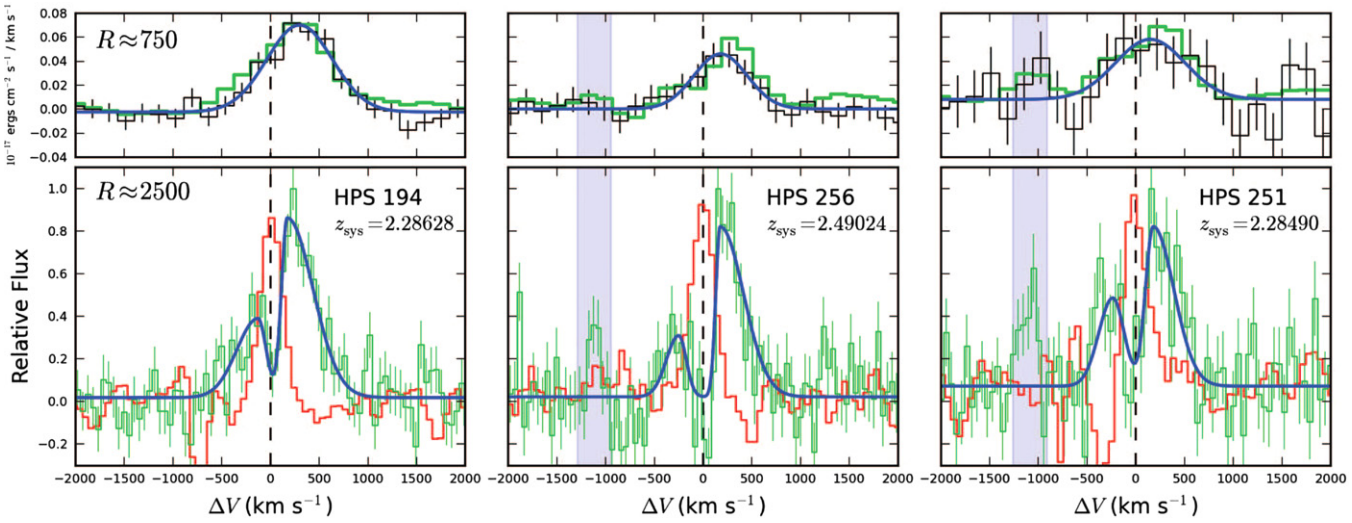

Figure 3. Lyα spectra of the three galaxies shown in velocity space. In the lower panels, we show the $R \approx 2500$ Lyα spectra as the thin green histogram. The blue curves in these panels represent the multi-component asymmetric Gaussian fits, as discussed in Section 3.2. The red histogram shows the Hα spectra for each object from M. Song et al. (2013, in preparation). The top panels show the co-added $R \approx 750$ HPS spectra for each galaxy in black along with Gaussian fits to the emission lines in blue. For comparison, we also show the $R \approx 2500$ Lyα spectra after being degraded to the HPS spectral resolution in green. The light blue shaded region in the HPS256 and HPS251 panels indicates the location of the second blueshifted peak examined in Section 3.2.1.

(A color version of this figure is available in the online journal.)

insensitive to the specifics of the data combination procedure. Thus, we do not believe that the peaks at -1000 km s^{-1} for HPS256 and HPS251 are the result of systematic or random effects in the $R \approx 2500$ data.

We look to the distribution of the sources on the sky within the extent of the fiber by examining the COSMOS *V*-band images shown in Figure 1. Both of our primary targeted galaxies (i.e., HPS194 and HPS256) are centered within the fiber with no additional continuum sources located within the rms positional error. The case for HPS251 is more complicated. Since it was not originally a primary target of our observations, the location of the LAE continuum counterpart is not positioned optimally with respect to the fiber center. As a result, the area of sky covered by the fiber contains several additional continuum sources. These include a brighter and extended source with a photometric redshift[10] of $0.97^{+0.04}_{-0.05}$ (Ilbert et al. 2009). If the second HPS251 blue peak was from this lower-redshift galaxy, its rest-frame wavelength would be 2019^{+53}_{-40} Å. Since this range does not correspond to any prominent near-UV transition, the low-redshift galaxy in the fiber is most likely not the source of the second blue peak[11]. The remaining source other than the LAE itself within the fiber (taking into account the rms uncertainty in its position) is a faint source to the east of the low-redshift galaxy. This source has no COSMOS photometric redshift.

Since we are unable to definitively determine another source from which they originate, we cannot rule out that the second blueward peaks are indeed Lyα emission from the targeted LAEs. A triple-peaked Lyα line displaying two weak blue peaks has not been previously observed in studies that looked for multiple-peaked Lyα emission (e.g., Kulas et al. 2012; Yamada et al. 2012). Additionally, there are no clear examples of such highly blueshifted Lyα emission, even in the most extreme starburst LAEs in the nearby universe when observed with high resolution and sensitivity (see Heckman et al. 2011). With the inconclusive nature of the second blue peaks and given the prevalence of "Group 1"-type double-peaked profiles in the literature, we continue forward treating HPS256 and HPS251 as double-peaked objects (i.e., we ignore the second blueward peaks). However, we will return to the possibility of these galaxies being more complex, triple-peaked Lyα systems in Section 5.

3.2.2. Quantitative Description of the Lyα Emission

To quantitatively characterize the Lyα line profiles and extract observable quantities from the double-peaked profiles, we utilize the MPFIT IDL package (Markwardt 2009) to fit a function $f_{\rm tot}(\Delta v)$ to each galaxy's Lyα spectrum in velocity space with the following form:

$$f_{\rm tot}(\Delta v) = f_{\rm blue}(\Delta v) + f_{\rm red}(\Delta v) + C, \quad (1)$$

where C is the continuum level and $f_x(\Delta v)$ is a function describing each component of emission (e.g., f_x denotes the red emission component if $x = red$ and the blue component if $x = blue$). At the spectral resolution of our data, the emission components are asymmetric. For $f_x(\Delta v)$, we thus adopt an "asymmetric Gaussian[12]" functional form similar to that used by McLinden et al. (2011) to fit the Lyα line profiles of $z = 3.1$ LAEs. This is given by

$$f_x(\Delta v) = A_x \ \exp\left[-\frac{(\Delta v - \Delta v_{0,x})^2}{2\sigma_x^2}\right], \quad (2)$$

where A_x is the amplitude of the respective emission component above the continuum level, $\Delta v_{0,x}$ is the velocity of the peak emission of the component, and σ_x is a width parameter. Skew is introduced to the Gaussian described above by defining σ_x as

$$\sigma_x \equiv \begin{cases} \sigma_{x,b} & \text{if } \Delta v < \Delta v_{0,x} \\ \sigma_{x,r} & \text{if } \Delta v > \Delta v_{0,x} \end{cases}.$$

[10] COSMOS Photometric Redshift Catalog, 2008 November Release. The quoted uncertainties correspond to the 99% confidence interval.

[11] The photometric redshift of this brighter and extended source is confirmed with a detection of Hα at 12989 Å ($z = 0.98 \pm 0.01$) in the 3D-HST survey (Brammer et al. 2012).

[12] The "asymmetric Gaussian" function is implemented in our IDL code through the `ARM_ASYMGAUSS` routine developed by Andrew Marble: http://hubble.as.arizona.edu/idl/arm/.

Table 2
Best-fit $R \approx 2500$ Lyα Observables

Parameter	Units	HPS194	HPS256	HPS251
$F_{\rm red}/F_{\rm blue}$	···	2.4 ± 0.4	$3.9^{+0.9}_{-1.2}$	$2.0^{+0.7}_{-0.4}$
$\Delta v_{0,\rm red}$	km s^{-1}	173^{+17}_{-20}	175^{+9}_{-19}	179^{+8}_{-28}
$\Delta v_{\rm tot}$	km s^{-1}	300^{+19}_{-71}	425^{+33}_{-38}	415^{+29}_{-44}
FWHM$_{\rm blue}$	km s^{-1}	353^{+48}_{-62}	240^{+75}_{-23}	306^{+81}_{-37}
FWHM$_{\rm red}$	km s^{-1}	380^{+44}_{-23}	335^{+11}_{-80}	343^{+45}_{-18}
$\alpha_{\rm blue}$	···	$0.4^{+0.1}_{-0.2}$	$0.6^{+0.4}_{-0.1}$	0.8 ± 0.2
$\alpha_{\rm red}$	···	$4.4^{+1.2}_{-0.9}$	$5.3^{+1.5}_{-0.5}$	$2.7^{+0.8}_{-0.1}$

Notes. See Section 3.2 for the definitions of these parameters. The quoted uncertainties are statistical. Systematic errors associated with the optical and NIR wavelength calibrations are discussed in Sections 2.2 and 2.3.1, respectively (these only affect the $\Delta v_{0,\rm red}$ measurement).

The FWHM of component x is then given by

$$\mathrm{FWHM}_x = \sqrt{2\ln(2)}\,(\sigma_{x,b} + \sigma_{x,r}), \quad (3)$$

and we define a parameter describing the skew as

$$\alpha_x \equiv \sigma_{x,r} \,/\, \sigma_{x,b}. \quad (4)$$

This parameter is defined such that $\alpha_x = 1$ describes a symmetric emission component, while $\alpha_x > 1$ (<1) describes an asymmetric emission component with an extended red (blue) tail. We extract a total of seven observables describing the Lyα line profile morphology: the red-to-blue component flux ratio $F_{\rm red}/F_{\rm blue}$ (where $F_x = \int f_x(\Delta v)\ d(\Delta v)$), the red component velocity offset from systemic ($\Delta v_{0,\rm red}$), the total velocity separation of the red and blue components ($\Delta v_{\rm tot} = \Delta v_{0,\rm red} - \Delta v_{0,\rm blue}$), FWHM$_{\rm blue}$, FWHM$_{\rm red}$, $\alpha_{\rm blue}$, and $\alpha_{\rm red}$. We do not include C since the continuum flux for all three galaxies is well below the detection limit of our spectra. Note that the functional form of $f_{\rm tot}(\Delta v)$ is not motivated by the physics of the Lyα radiative transfer, but is rather for the purpose of parameterizing the emission line morphology for comparison with previously published results. This fitting procedure will be especially useful in the future for characterizing and finding trends in large samples of observed Lyα emission line profiles.

In the bottom panels of Figure 3, we show the best-fit $f_{\rm tot}(\Delta v)$ to each Lyα emission line, the parameters of which are listed in Table 2. The quoted statistical uncertainties encompass the 68% confidence interval and were determined by fitting Equation (1) to 10^3 Monte Carlo realizations of the observed spectrum, similar to the method described in Section 3.1 for the low-resolution HPS Lyα spectra. In addition to these statistical uncertainties, recall that there also exists a systematic uncertainty in the velocity zero point resulting from the NIR data (see Section 2.3.1; this only affects the $\Delta v_{0,\rm red}$ measurement). All applicable values reported in Table 2 (i.e., FWHM$_x$ and α_x) have not been corrected for the instrumental resolution. Such a correction would decrease the FWHM$_x$ measurements (by no more than 30 km s^{-1} for the narrowest component) and increase (decrease) the $\alpha_{\rm red}$ ($\alpha_{\rm blue}$) measurements, thus yielding the asymmetry parameterizations as lower (upper) limits. As a result, these limits on α_x clearly indicate that the red Lyα peak for each LAE is quite asymmetric with a red tail, while the blue Lyα peak tends to be asymmetric with a blue tail.

One may notice that the measured $\Delta v_{0,\rm red}$ given in Table 2 may not necessarily agree with the $\Delta v_{\rm ly\alpha}$ measurements from the lower resolution HPS observations in Table 1. This is due to the low S/N of both sets of spectra and the intrinsic asymmetry in the dominant redward Lyα emission peak (in particular, the extended red tail and truncated blue edge of that component). When observing such an asymmetric emission line at the lower spectral resolution of the HPS, the excess emission in the extended red tail pulls the convolved peak of the unresolved line further redward. This can be seen in the top panel of Figure 3 when comparing the actual HPS $R \approx 750$ data with the $R \approx 2500$ data that have been degraded to the HPS spectral resolution and dispersion. We discuss this effect further in Section 5.4.

3.3. Double-peaked Lyα Emission across Galaxy Samples

The presented sample of three LAEs were *not* preselected to have multiple Lyα emission components. However, it should not be surprising that each LAE shows a multiple-peaked morphology at high spectral resolution since multiple peaks are a natural outcome of Lyα resonant line transfer. This is due to photons diffusing through the scattering medium in real and frequency space until reaching the line wings on either side of the core where the optical depth is low enough for escape. For the simplest case of resonant scattering through static gas, the result is a double-peaked emergent spectrum that is symmetric about the velocity zero point (Neufeld 1990). The observed frequency of multiple peaked Lyα emission appears to be significant for LAE samples (∼50% in the overdense SSA22-Sb1 field; Yamada et al. 2012) as well as for LBG samples (∼30%; Kulas et al. 2012). These frequencies should be regarded as lower limits due to the limited spectral resolution and S/N of the data. Disregarding possible trends with environment (i.e., overdensity versus field), these results suggest that drawing three LAEs with multiple peaks from the HPS sample is not an unlikely scenario.

At low spectral resolution, the measured velocity offsets of all three LAEs in our sample appear to be consistent with the mean Lyα velocity offset as measured from eight other Lyα-selected galaxies in the literature that were observed at similar resolution ($\langle \Delta v_{\rm Ly\alpha} \rangle = 164 \pm 97$ km s^{-1}, where the uncertainty represents the standard deviation of the sample; McLinden et al. 2011; Hashimoto et al. 2013; Guaita et al. 2013). This value, as noted by Finkelstein et al. (2011) and the aforementioned authors, is much smaller than the ∼450 km s^{-1} offset that is typically measured for LBGs (e.g., Steidel et al. 2010).

From the results of Yamada et al. (2012) and Kulas et al. (2012), Lyα spectra having a strong red component and a weaker blue component are the most common multiple-peaked line profile morphology. Besides being observed in both Lyα-selected and UV-continuum-selected samples of galaxies, this line profile can be observed for galaxies spanning a variety of redshifts from local LBG analogs (Heckman et al. 2011) to galaxies beyond $z \sim 3$ (Tapken et al. 2007). In addition, it is not only observed emerging from individual galaxies (e.g., this work, McLinden et al. 2011; Kulas et al. 2012; Christensen et al. 2012; Yamada et al. 2012), but also from the large Lyα nebulae (i.e., Lyα blobs; LABs) that are often associated with protoclusters (Matsuda et al. 2006; Yang et al. 2011) and radio galaxies (Adams et al. 2009).

As with the unresolved Lyα velocity offsets $\Delta v_{\rm Ly\alpha}$ discussed above, the velocity offsets of the multiple peaks relative to the systemic velocity might be expected to be different between LAE and LBG samples. From Kulas et al. (2012), the average velocity offset for the red emission component of their "Group 1" line profiles is $\langle \Delta v_{0,\rm red} \rangle = 417 \pm 101$ km s^{-1} while the average total separation between the red and blue components is

$\langle \Delta v_{\rm tot} \rangle = 801 \pm 136$ km s^{-1}. On average for the LAEs presented here, these same measurements are smaller by a factor of $\sim$2 (cf. Table 2). This is visualized in Figure 4, which shows the average $R \approx 2500$ spectrum of our three LAEs plotted on the same velocity scale relative to $z_{\rm sys}$ as the composite spectrum of the 11 "Group 1" double-peaked LBGs from Kulas et al. (2012). Additionally, we show a composite spectrum of 29 single peaked LBGs from Steidel et al. (2010). The top panel shows the Lyα spectra normalized by the peak flux to accentuate differences in the velocity offsets, while the lower panel shows the same spectra normalized to the continuum[13] redward of the Lyα line to accentuate differences in the relative EW$_{\rm Ly\alpha}$ for each sample. In both panels, we show a degraded version of our LAE composite Lyα line profile that has the same average spectral resolution of Steidel et al. (2010) and Kulas et al. (2012) to show that the differences in the velocity structure between the samples are largely invariant with spectral resolution. This figure embodies a trend that higher EW$_{\rm Ly\alpha}$ objects tend to have smaller Lyα velocity offsets (e.g., Hashimoto et al. 2013). This trend is especially interesting since there is naturally some overlap between LBG and LAE samples; some LAEs, such as those presented in this work, have high EW$_{\rm Ly\alpha}$ and small Lyα velocity offsets, but are bright enough in the continuum to be considered LBGs in most surveys and have some physical properties that are similar to the typical LBG, such as stellar mass.

In addition to the three LAEs presented here, the number of Lyα line profiles displaying the strong red and weaker blue double-peaked morphology with a measure of $z_{\rm sys}$ has grown significantly (e.g., Fynbo et al. 2010; Steidel et al. 2010; McLinden et al. 2011; Yang et al. 2011; Heckman et al. 2011; Kulas et al. 2012; Christensen et al. 2012; Noterdaeme et al. 2012). As with our three LAEs, the systemic Lyα line center usually lies in between the two peaks. While the large sample of such Lyα line profiles from Yamada et al. (2012) for LAEs do not have a measure of $z_{\rm sys}$, these previous results suggest that we can be reasonably safe in at least comparing $\Delta v_{\rm tot}$ for our galaxies with that from the Yamada et al. (2012) sample. Since the Yamada et al. (2012) sample has $\langle \Delta v_{\rm tot} \rangle = 608 \pm 170$ km s^{-1}, our LAEs appear to be on the lower end of the distribution. However, despite the asymmetry that they measure in their Lyα spectra, Yamada et al. (2012) determine the peak-to-peak separation by fitting symmetric Gaussians to each emission component. If we were to fit our Lyα spectra with symmetric Gaussians consistent with their method, $\Delta v_{\rm tot}$ would be 422, 561, and 559 km s^{-1} for HPS194, HPS256, and HPS251, respectively. In this case, each of our LAE would be close to within 1σ of the mean of the Yamada et al. (2012) $\Delta v_{\rm tot}$ distribution. Thus, as also seen at lower resolution, our double-peaked Lyα spectra appear to be consistent with those already measured for other LAE samples.

Depending on the gas geometry and kinematics, the asymmetric shape of the emission line components can provide clues about the Lyα radiative transfer and the properties of the scattering gas (e.g., Verhamme et al. 2006; Zheng et al. 2010; Schaerer et al. 2011; Christensen et al. 2012; Noterdaeme et al. 2012). As seen from our measurements, both emission peaks in the three LAEs' spectra are typically asymmetric, with a sharper falloff toward the Lyα line center. While asymmetry measurements are highly dependent on the instrumental resolution, we can at least compare our Lyα spectra qualitatively to the asymmetry observed for galaxies showing Lyα with a similar characteristic double-peaked morphology. At slightly lower spectral resolution than our data (180 km s^{-1} FWHM as compared to our data at 120 km s^{-1}), Yamada et al. (2012) find that the stronger red peak in objects showing the characteristic double-peaked Lyα profile is typically asymmetric with an extended red wing on the red emission component. McLinden et al. (2011) also find this for the one object in their sample displaying the double-peaked morphology. At similar or higher spectral resolution to ours, studies such as Fynbo et al. (2010), Heckman et al. (2011), Yang et al. (2011), Noterdaeme et al. (2012), and Christensen et al. (2012) have observed objects whose double-peaked Lyα spectrum is asymmetric in the same manner as our spectra (i.e., each emission component showing asymmetry with the sharpest falloff toward line center). The asymmetry in our data appear to be consistent with that of the highest resolution Lyα spectra in the examples given ($\lesssim$75 km s^{-1} FWHM; Christensen et al. 2012), which shows that the flux falloff toward line center is extremely sharp. Such asymmetry is thought to be the signature of outflowing gas, where the extended red wing of the red emission component consists of photons that have been "backscattered" several times off of the far-side inner surface of an expanding shell of neutral hydrogen gas (e.g., Verhamme et al. 2006; also, see Section 4.2). In the following section, we examine the ability of such a model to reproduce the shape of the observed Lyα profiles for our LAEs.

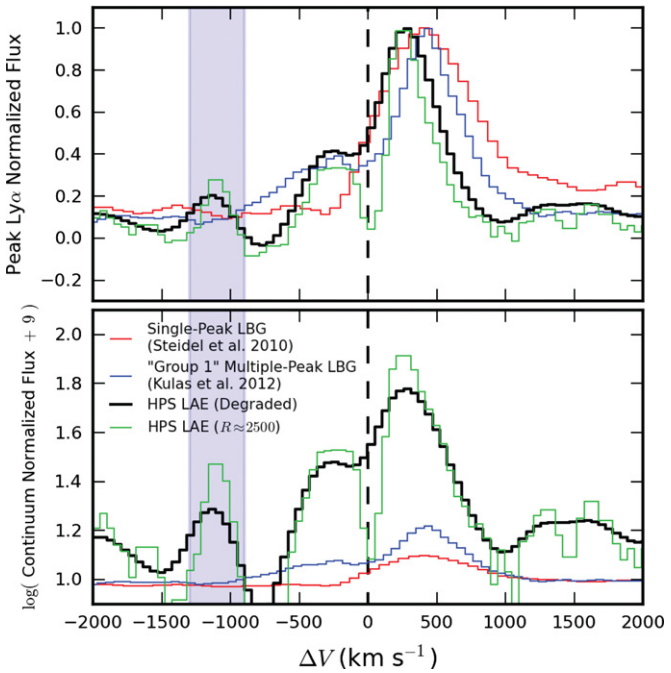

Figure 4. Comparison of the Lyα line profiles for different galaxy samples. In both panels, the blue histogram is the composite Lyα spectrum for LBGs from Kulas et al. (2012) that encompass the "Group 1" multiple-peaked profiles and qualitatively match the general Lyα morphology of the LAEs presented here. The red histogram is the composite spectrum of single-peaked Lyα profiles of LBGs from Steidel et al. (2010). The green histogram is the average $R \approx 2500$ Lyα line profile for the three HPS LAEs observed in this work, while the black histogram is the same data but degraded to the same spectral resolution as the LBG Lyα spectra. The top panel is normalized to the peak Lyα flux to accentuate differences in the velocity axis while the lower panel is normalized to the continuum flux redward of Lyα, showing the relative differences in EW$_{\rm Ly\alpha}$. The light blue shaded region has the same meaning as in Figure 3.

(A color version of this figure is available in the online journal.)

[13] The relative flux of our $R \approx 2500$ Lyα spectra has been scaled to match the total Lyα line flux measured from the HPS (Adams et al. 2011). Since no continuum is detected spectroscopically for our LAEs, we use the continuum flux measured by COSMOS V-band photometry for normalization (see Table 1).

4. COMPARISON WITH Lyα RADIATIVE TRANSFER MODELS

In Section 1 and the references therein, the complex processes that govern the escape of Lyα from a galaxy and their effect on the emergent Lyα emission line profile were discussed, along with mention of several studies which attempt to model them. To date, the model that observed Lyα line profiles have been most widely compared with is that of the propagation of Lyα photons through a simple expanding, spherical shell of neutral hydrogen gas (e.g., Verhamme et al. 2006; Barnes & Haehnelt 2010; Schaerer et al. 2011). This is largely due to its success in reproducing many observed properties of $z \sim 3$ LBGs, including the shape of the Lyα line in emission and absorption for various line profile morphologies (e.g., Schaerer & Verhamme 2008; Verhamme et al. 2008). While highly idealized, this model is physically motivated by the basic picture of a star-forming galaxy in which the energy from a centrally located starburst (which is the location of the initial Lyα emission) pushes out the ISM through the combined effect of stellar winds and supernovae explosions. The result is a "superbubble" formed within a geometrically thin shell of expanding neutral gas.

4.1. The Expanding Shell Model Grid

To compare with the $R \approx 2500$ data, we have used the Lyα radiative transfer code developed by Zheng & Miralda-Escudé (2002) and Kollmeier et al. (2010) to produce a grid of model Lyα spectra resulting from the transfer of Lyα photons through expanding, isothermal, and homogeneous shells of neutral hydrogen gas. This code was also used by Kulas et al. (2012) in their qualitative comparison of model Lyα line profiles with the multiple-peaked Lyα spectra of LBGs. The expanding shell radiative transfer models that we run are identical to previous work by Verhamme et al. (2006) and Schaerer et al. (2011), with the exception of a couple notable simplifications.

1. *Intrinsic Lyα spectrum.* The intrinsic spectrum emitted from the central point source in these two studies is a Gaussian Lyα line plus a continuum, whereas our models currently only use an idealized monochromatic Lyα line. The lack of continuum emission in our models results in only negligible effects on the output model Lyα spectra since we are comparing them with the Lyα spectra of galaxies that have observed $\mathrm{EW}_{\mathrm{Ly}\alpha} > 100$ Å in the rest frame. Using Hα, M. Song et al. (2013, in preparation) have measured the 1D integrated line-of-sight nebular velocity dispersion $\sigma_{\mathrm{H}\alpha}$ for each galaxy. This traces the velocity dispersion of the galaxy's H II regions and thus the width of the intrinsic Lyα emission. For the three LAEs presented here, $\sigma_{\mathrm{H}\alpha}$ is at most 72 km s^{-1} (which is systematically smaller by ∼40 km s^{-1} than $\sigma_{\mathrm{H}\alpha}$ for the average $z \sim 2$ UV-selected galaxy; Erb et al. 2006). We discuss the effect of using a dispersion of Lyα injection frequencies (rather than a monochromatic line) in Section 5.1.
2. *Dusty shells.* The neutral hydrogen shells in these two studies can be uniformly mixed with dust (parameterized by a dust absorption optical depth τ_a, which essentially characterizes the dust-to-gas ratio), whereas we model only dust-free shells. Including dust in the shell has the effect of "sharpening" the Lyα line profile. Basically, this is because photons that emerge farther from the Lyα line center have encountered more scattering events, which gives them a higher probability of being absorbed by a dust grain. For $\tau_a \lesssim 1$, the overall shape of the emergent Lyα line profile is well preserved when compared to the dust-free line profile emerging from an otherwise identical shell, other than the sharpening effect (Verhamme et al. 2006; Schaerer et al. 2011). The dust absorption optical depth is related to the measured extinction as $E(B-V) \approx 0.1\tau_a$ (Verhamme et al. 2006). Using $E(B-V)$ for our three LAEs (cf. Table 1; Blanc et al. 2011), $\tau_a \approx 0.9 \pm 0.6$, 1.0 ± 0.9, and 0.7 ± 0.8 for HPS194, HPS256, and HPS251, respectively. The potential impact of dust on our comparison with dust-free shell models is further discussed in Section 5.1.

An individual model on our grid is thus characterized by three parameters that describe the shell: the (uniform) expansion velocity V_{exp}, the Doppler parameter b (which in the absence of turbulence is equivalent to the gas thermal velocity), and the neutral hydrogen column density $N_{\mathrm{H\,I}}$. Our grid has been computed for the following values: $V_{\mathrm{exp}} = 50$, 100, 200, and 300 km s^{-1}; $b = 20$, 40, 80, and 120 km s^{-1}; $N_{\mathrm{H\,I}} = 10^{17}$, 10^{18}, 10^{19}, and 2×10^{20} cm^{-2}. For comparison with the $R \approx 2500$ Mitchell Spectrograph Lyα data, each model Lyα spectrum has been convolved with a 120 km s^{-1} FWHM Gaussian kernel.

4.2. Model Trends

Verhamme et al. (2006) decompose the Lyα line profile to determine how various features in multiple-peaked Lyα spectra arise (see their Figure 12). In summary, there are three basic modes of escape of Lyα photons from an expanding shell, any number of which could be occurring simultaneously in the same model depending on the shell parameters: (1) a single series of scatterings before escape, (2) one or more series of "backscatterings" before escape (where a backscattering event is defined as a series of scatterings after which the photon traverses the shell's cavity and reenters the shell in a different location), and (3) direct escape (i.e., no interaction with the shell). Mode 1, which is a similar process to resonant scattering through a slab of neutral gas, results in a peak blueward of the Lyα line center *and* a redward peak. The relative strength of these two peaks is determined by V_{exp} (i.e., the two peaks are more equal in strength for small V_{exp} as one approaches the static case). Mode 2 results in *another* peak redward of the Lyα line center, which is composed of photons that have undergone one backscattering event. Due to radiative transfer effects (i.e., these photons are "reflected" off the receding inner surface of the shell back toward the observer), this peak traces $\sim 2V_{\mathrm{exp}}$ in terms of its offset from the line center. Photons that undergo more than one backscattering event emerge progressively redward of this peak with less probability, which results in an extended redward tail. Finally, mode 3 occurs only when V_{exp} is large enough for the Lyα photons emitted at the shell's center to already be redshifted out of resonance in the frame of the expanding gas when they encounter the shell. Therefore, these photons emerge as a peak at the Lyα line center.

In Figure 5, we show several representative model Lyα spectra from the grid, where each panel shows the variation of one of the three parameters for fixed values of the other two about a fiducial model having $N_{\mathrm{H\,I}} = 10^{19}$ cm^{-2}, $b = 80$ km s^{-1}, and $V_{\mathrm{exp}} = 100$ km s^{-1}. All of the escape modes discussed above are seen in at least one of the models shown in this figure.

To understand how the Lyα line profile that is emergent from the expanding shell depends on the three parameters, we begin by considering the simplest case of resonant scattering through a static slab of neutral hydrogen gas with Doppler parameter b

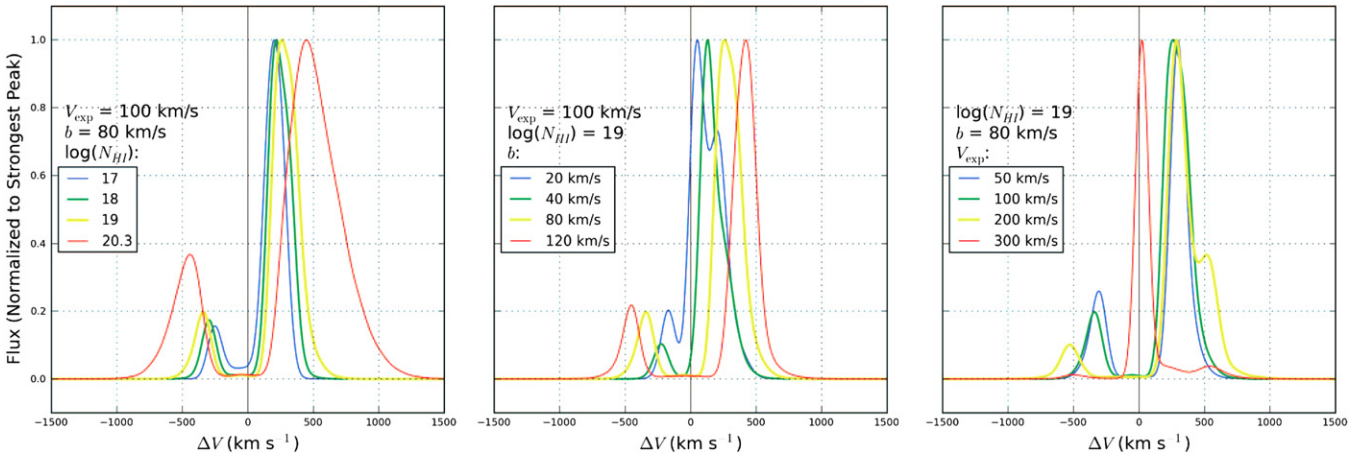

Figure 5. Representative Lyα emission line profiles from the grid of Lyα radiative transfer models in the homogeneous expanding shell geometry. From left to right, each panel shows the variation of the Lyα emission line profile as functions of $N_{\rm H\,I}$, b, and $V_{\rm exp}$, respectively, while the other two respective parameters are held constant about a fiducial model having $N_{\rm H\,I} = 10^{19}$ cm^{-2}, $b = 80$ km s^{-1}, and $V_{\rm exp} = 100$ km s^{-1}. Each model spectrum has been convolved with a 120 km s^{-1} FWHM Gaussian kernel for comparison with our $R \approx 2500$ Mitchell Spectrograph observations of Lyα and have been scaled to the peak flux.

(A color version of this figure is available in the online journal.)

and neutral hydrogen column density $N_{\rm H\,I}$. This configuration results in a symmetric double-peaked spectrum about the Lyα line center (e.g., Neufeld 1990). Based on a random walk in both frequency space and real space, one can show that the typical velocity offsets of the peaks from the line center are approximated by (e.g., Hansen & Oh 2006; Verhamme et al. 2008)

$$\Delta v \sim \pm 190 \left[\mathrm{km\ s^{-1}}\right] \left(\frac{b}{80\ \mathrm{km\ s^{-1}}}\right)^{1/3} \left(\frac{N_{\rm H\,I}}{10^{19}\ \mathrm{cm^{-2}}}\right)^{1/3}. \quad (5)$$

Imparting a bulk velocity to the slab toward the observer (away from the Lyα source) results in a growing asymmetry in the flux of the two peaks as the Lyα photons upon the first interaction are redshifted in the frame of the hydrogen atoms. As a result, bluer photons shift into resonance, which diminishes the bluer peak relative to the redder peak. When the slab has a bulk velocity, the velocity offsets of the emission peaks are no longer well approximated by the relation in Equation (5), but the basic behavior remains the same (i.e., the total separation between the peaks increases with increasing b and $N_{\rm H\,I}$). This scenario qualitatively describes escape mode 1 for photons escaping the expanding shell on the hemisphere approaching the observer at $V_{\rm exp}$, and the basic trends described above can be seen in the panels of Figure 5.

As mentioned, escape modes 1 and 2 together result in two emission peaks redward of the Lyα line center. While several models in Figure 5 show this morphology, the majority only show a single redward peak. As noted by Verhamme et al. (2006), decreasing the ratio $V_{\rm exp}/b$ results in these two red peaks becoming increasingly superposed, eventually resulting in a single blended redward emission peak. Decreasing this ratio also results in a decrease of the ratio of the flux redward of the line center to the blueward flux. This is in part due to the move closer to the static case with decreasing $V_{\rm exp}$.

Changes in $N_{\rm H\,I}$ result in complex variations of the line profile. In general, as roughly described by Equation (5), increasing $N_{\rm H\,I}$ results in an increased separation between the peaks. Additionally, the FWHM and asymmetry of each peak increases with increasing $N_{\rm H\,I}$ due to the photons needing to scatter farther out into the line wings in order to escape the optically thick column, especially for the redward emission as the mode 2 backscattering effect is increased. This is also the cause of the decreasing ratio of the flux redward of the line center to the blueward flux for a given $V_{\rm exp}$. As mentioned above, the velocity offset of the red peak that results from escape mode 2 (i.e., backscattered photons) typically traces $\sim 2V_{\rm exp}$. At first glance, this feature of the emergent Lyα line profile seems to provide a tight constraint on the outflow velocity of the system. However, we have mentioned that this peak can become blended with the redward peak resulting from escape mode 1 for decreasing $V_{\rm exp}/b$. To further complicate the matter, Verhamme et al. (2006) note that the redward peak from escape mode 1 decreases in strength relative to the escape mode 2 peak with increasing $N_{\rm H\,I}$. This effect is clearly illustrated in Figure 17 of Verhamme et al. (2008), which shows how the velocity offset of the *dominant* redward Lyα peak traces a varying multiplicative factor of $V_{\rm exp}$ with various values of $N_{\rm H\,I}$. For $N_{\rm H\,I} \gtrsim 10^{20}$ cm^{-2}, the most dominant of the two redward peaks results from the backscattered escape mode 2 photons and traces $\sim 2V_{\rm exp}$. For smaller $N_{\rm H\,I}$, the dominant redward peak results from escape mode 1 photons and its velocity offset traces $< 2V_{\rm exp}$. This explains why little change in the velocity offset of the dominant red peak in the right panel of Figure 5 is seen with changing $V_{\rm exp}$. Since the models we show are for $N_{\rm H\,I} = 10^{19}$ cm^{-2}, the dominant peak results from escape mode 1 photons whose velocity offset from the line center is primarily determined by changes in $N_{\rm H\,I}$ and b (cf. Equation (5)). $N_{\rm H\,I}$ is particularly dominant because, in addition to shifting the emission components in velocity, it has the ability to strongly influence the FWHM and asymmetry of the emission components. Additionally, its dynamic range is much larger than that for b.

As can be seen by the above discussion and the example model spectra shown in Figure 5, the emergent Lyα line profile changes in non-trivial fashion for variations in each individual parameter. In addition, simple qualitative interpretations of observed Lyα line profiles under the expanding shell model can be hindered by the degeneracies of the modeling parameters on all observables (e.g., one needs to constrain $N_{\rm H\,I}$ before using the velocity offset of the dominant redward peak directly as a tracer of

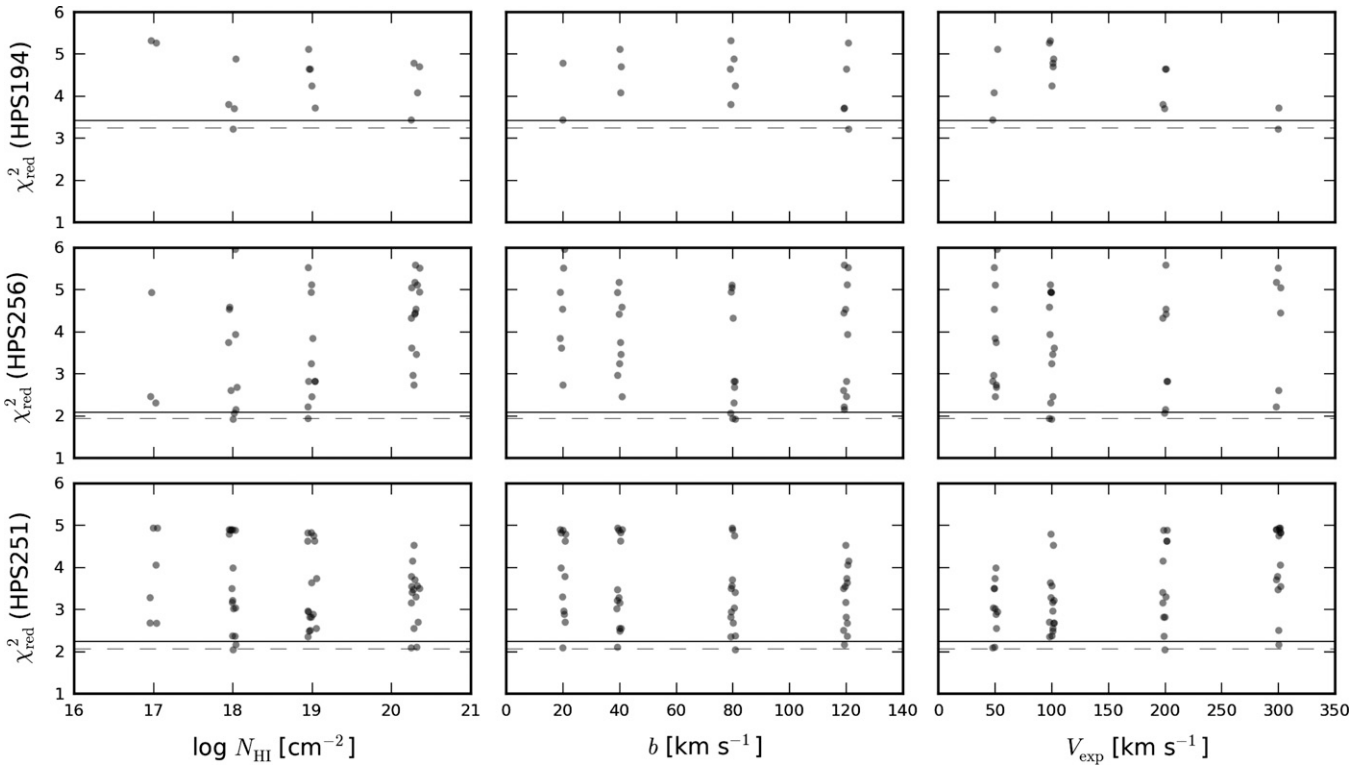

Figure 6. Results of the statistical comparison of the Lyα spectra of the three LAEs with the grid of model Lyα line profiles in the expanding shell geometry. The reduced χ^2 statistic ($\chi^2_{\rm red}$) is shown as a function of each of the three model parameters. In each panel, the horizontal dashed and solid lines represent the 68% and 99% confidence limits shown in the reduced units, respectively. To emphasize the minimum $\chi^2_{\rm red}$ model, the vertical axis of each panel is set such that models with $\chi^2_{\rm red} > 6$ are not shown. Each data point has been scrambled by a small, random amount along the horizontal axis and displayed with some degree of transparency to avoid confusion between similarly valued points.

$V_{\rm exp}$). While such constraints are not currently available for our galaxies, our observed Lyα spectra are of sufficient resolution to identify individual emission components and their shapes (i.e., asymmetries, widths, etc.). By conducting a statistical comparison of our observed Lyα spectra with the spectra of the expanding shell model grid, we aim to constrain the physical parameters of the gaseous component of the LAEs through which the Lyα photons scatter.

4.3. Statistical Comparison with Observed Lyα

We perform a statistical comparison between the observed Lyα emission line profiles and the expanding shell Lyα radiative transfer models by calculating the χ^2 statistic for each model on the grid for each galaxy. After being degraded to the instrumental resolution, each model in the grid is interpolated via cubic spline to the velocity bin centers of each galaxy's observed Lyα spectrum. The observed spectra are corrected for the background level C measured in Section 3.2.2 (this is important only for HPS251, which includes faint continuum from the nearby extended low-redshift galaxy that was within the fiber; see Figures 1 and 3). Finally, we multiply the model by a scaling factor A, which is determined by minimization of the squared residuals between the model and the data. We calculate the χ^2 statistic as follows:

$$\chi^2 = \sum_{i=1}^{N} \left[\frac{F_i - y\,(N_{\rm H\,I},\ b,\ V_{\rm exp},\ A;\ \Delta v_i)}{\sigma_i} \right]^2, \quad (6)$$

where F_i and σ_i are the observed relative flux and its associated statistical uncertainty, respectively, each at the ith velocity bin Δv_i. Here, the model spectrum with the parameters $N_{\rm H\,I}$, b, $V_{\rm exp}$, and A, is denoted as y. Recall that there is an uncertainty on the velocity zero point of the observed Lyα spectrum that results from the rms of the Mitchell Spectrograph and NIRSPEC wavelength solutions as well as the systematic uncertainty associated with the $z_{\rm sys}$ measurement (see Sections 2.2 and 2.3.1). To reflect this uncertainty in our analysis, we have allowed the observed Lyα spectra to shift relative to the velocity zero point within this total uncertainty until the minimum χ^2 is found for each model on the grid. The total uncertainty in the velocity zero point is ± 19, ± 20, and ± 21 km s^{-1} for HPS194, HPS256, and HPS251, respectively.

For a common comparison of the calculated χ^2 values between the three galaxies, we calculate the reduced χ^2 statistic, which is given by $\chi^2_{\rm red} = \chi^2/(N - M)$, where N is the number of velocity bins in each spectrum and M is the number of degrees of freedom (here, $M = 5$). Since we only included data in the range $-1000 < \Delta v\ ({\rm km\ s^{-1}}) < 1000$ in our calculation of χ^2 (i.e., we ignore the second blueward peak in HPS256 and HPS251), N is 38, 44, and 39 for HPS194, HPS256, and HPS251, respectively.

In Figure 6, we show the results of the statistical comparison of the $R \approx 2500$ data with the expanding shell model grid by plotting $\chi^2_{\rm red}$ as a function of each of the three physical model parameters for each galaxy. We include horizontal lines that represent the $\Delta\chi^2$ above the minimum χ^2 for each galaxy in the reduced units that corresponds to the 68% and 99% confidence limits (Press et al. 1992). As can be seen from Figure 6, the data appear to be able to constrain the models relatively well at the 68% confidence level. For HPS194 and HPS251, a single best-fit model lies below the 68% confidence limit. For HPS256, two models lie below the 68% confidence limit, although these two

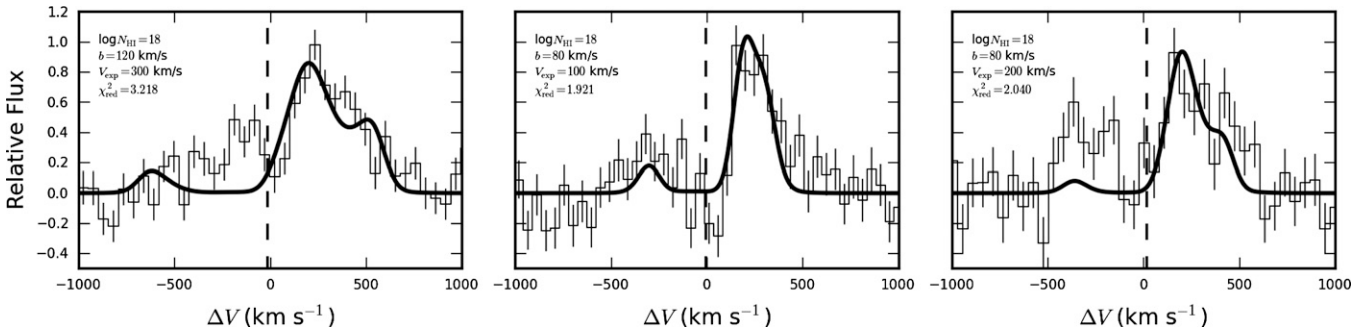

Figure 7. Observed Lyα spectra of the three LAEs plotted with their respective best-fitting expanding shell model Lyα spectra. The magnitude of the velocity shift within the total velocity zero point uncertainty that yields the minimum χ^2 is visualized in these panels by the shifted vertical dashed line relative to $\Delta v = 0$ km s^{-1}. The best-fitting models and their respective statistics are listed in Table 3.

Table 3
Summary of Best-fit Expanding Shell Models

Object	$N-M$	Q	log $N_{\rm H\,I}$	b (km s^{-1})	$V_{\rm exp}$ (km s^{-1})	$\chi^2_{\rm red}$
HPS194	33	4.1×10^{-10}	18	120	300	3.218
HPS256	39	7.8×10^{-4}	18	80	100	1.921
HPS251	34	3.2×10^{-4}	18	80	200	2.040

Notes. The models listed are the best fit at the 68% confidence level, with the exception of HPS256. For HPS256, a model with the same b and $V_{\rm exp}$ (but with $N_{\rm H\,I} = 10^{19}$ cm^{-2}) is the next best fit. Since these two models differ by $\Delta\chi^2 = 0.61$, they both lie within the 68% confidence limit.

models occupy nearly same position in the three-dimensional (3D) parameter space and differ only by one order of magnitude in $N_{\rm H\,I}$. At the 99% confidence level, HPS194 still only has a single best-fitting model. HPS256 and HPS251, however, have three and four models lying below the 99% confidence limit, respectively, and are thus less well constrained. In particular, the lower S/N of the HPS251 Lyα spectra resulted in the four models within the 99% confidence limit spanning the entire parameter space in both b and $V_{\rm exp}$.

The best-fit models for each galaxy are summarized in Table 3 and are plotted with the $R \approx 2500$ Lyα data in Figure 7. From this figure, we can qualitatively state that the emission redward of the Lyα line center is relatively well represented by the expanding shell model spectra for each galaxy except for the extended red wings for HPS256 and HPS251. The emission blueward of the Lyα line center, however, is very poorly fit by the best-fitting model for each galaxy except for HPS256. For HPS194 and HPS251, the models do not reproduce the proper velocity offset or red-to-blue peak flux ratio. To estimate the probability of the observed residuals being due to statistical fluctuations in the data, we have calculated the probability Q, which is given by the integral of the χ^2 probability density function for $N-M$ degrees of freedom, integrated from the best-fit χ^2 value for each galaxy to infinity (Press et al. 1992). We obtain probabilities of 4.1×10^{-10}, 7.8×10^{-4}, and 3.2×10^{-4} for HPS194, HPS256, and HPS251, respectively. This suggests that even the best-fitting expanding shell model Lyα spectra are relatively poor representations of the observed Lyα spectra for these galaxies.

5. DISCUSSION

5.1. Possible Limitations of Our Models

In Section 4.1, we discussed the differences between our homogeneous expanding shell models and those of Verhamme et al. (2006) and Schaerer et al. (2011). The differences are the simplification of the input spectrum and the lack of dust. We discuss each of these below as they pertain to the statistical comparison presented above.

We have already stated that the lack of continuum is negligible in our models since our objects have such high EW$_{\rm Ly\alpha}$. However, all three galaxies have a measurable value of $\sigma_{\rm H\alpha}$ from the spectrally resolved Hα emission (M. Song et al. 2013, in preparation). Assuming the Lyα photons are originally emitted from the same gas that is emitting the detected Hα, these measurements imply an intrinsic Lyα FWHM of 144 ± 22, 170 ± 22, and 104 ± 14 km s^{-1} for HPS194, HS256, and HPS251, respectively. A higher intrinsic Lyα line width (as opposed to the monochromatic line we model) results in more photons beginning the resonant scattering process further from the core of the scattering cross-section. In non-static media, however, the frequency of the resonant core is shifted in the frame of the scattering gas. Thus, for the expanding shells we model, a non-monochromatic intrinsic Lyα line increases the direct escape probability of photons originally emitted redward of the Lyα line center while decreasing the corresponding probability for blueward emitted photons. The result is a slightly broader Lyα spectrum with similar velocity offsets and a slightly increased value of $F_{\rm red}/F_{\rm blue}$. A broader emergent Lyα spectrum would aid in fitting the extended red wings of the redward emission component for HPS256 and HPS251. However, this improvement may be negatively offset because, as seen in Figure 7, the flux ratio $F_{\rm red}/F_{\rm blue}$ is consistently too large in the models. In addition, a non-monochromatic intrinsic Lyα emission line would not significantly change the model emission component velocity offsets. Since the velocity offset of the HPS194 and HPS251 blueward emission component is already reproduced incorrectly by Lyα photon transfer through the expanding shell, including a frequency distribution rather than monochromatic Lyα photons would likely result in only negligible improvements for those objects.

As seen in Section 4.1, each LAE contains potentially significant amounts of dust (although the large uncertainties on $E(B-V)$ are also consistent with very little or no dust; Blanc et al. 2011). Verhamme et al. (2006) discuss how the various features of the Lyα line profile that arise from the various escape modes (see Section 4.2) change with increasing dust optical depth τ_a. In general, the photons that encounter more scatterings have a higher probability of being absorbed by dust due to their longer effective path length through the system. Thus, the backscattered photons of escape mode 2, particularly the extended red tail resulting from multiple backscattering events, are especially affected by dust which results in a more

narrow (or "sharpened") line profile (also, see Laursen et al. 2009). Additionally, the photons emerging blueward of the line center (i.e., the bluer photons resulting from escape mode 1 scatterings through the hemisphere of the shell expanding toward the observer) are also especially susceptible to dust absorption. This is because the bluer photons are redshifted closer to the resonant frequency as seen by the hydrogen atoms in the shell and undergo a larger number of core scatterings before emerging blueward enough for escape. These effects can be seen in Figure 17 of Verhamme et al. (2006), Figures 5 and 6 of Schaerer et al. (2011), and Figure 16 of Duval et al. (2013). As mentioned above, the expanding shell models within the searched parameter space do not reproduce the observed values of $F_{\rm red}/F_{\rm blue}$, with the peak blueward of the line center ubiquitously having too little flux in the best-fit models. Since the blueward peak is one of the features that is most easily extinguished by dust, including dust in our models cannot improve the best-fitting values of χ^2 since the little flux in the models blueward of the line center would only be further diminished.

As is often the case at $2 \lesssim z \lesssim 3$, we have ignored the effect of absorption and scattering in the IGM. While its effect is mostly to further diminish the Lyα emission that is blueward of the Lyα line center (e.g., Laursen et al. 2011), it is possible for gravitational inflow of IGM material in the vicinity of the galaxy's dark matter halo to also diminish the redward emission (Dijkstra et al. 2006b). However, since the mean optical depth of the IGM is $\lesssim$0.2 at the redshifts of the galaxies included in this study (Becker et al. 2013), we do not consider it as a contributing factor in the poor fits to the data.

Finally, we reiterate that we have modeled Lyα radiative transfer through expanding shells with a *homogeneous* distribution of neutral gas. Duval et al. (2013) have modeled Lyα radiative transfer through expanding shells with varying degrees of density inhomogeneity, from the homogeneous case to a scenario where all of the neutral gas is contained in clumps (i.e., the volume in the shell between the clumps is transparent to Lyα photons). In general, they find that the overall shape of the emergent Lyα line profile for increasing degrees of inhomogeneity is basically unchanged and follows the same trends as seen in the homogeneous case (see Section 4.2 and Verhamme et al. 2006). However, one marked change for parameter combinations resulting in double-peaked spectra (i.e., models with low $V_{\rm exp}/b$) is the reduction in $F_{\rm red}/F_{\rm blue}$ with increasing inhomogeneity. As seen in Figure 13(b) of Duval et al. (2013) for an expanding shell with $N_{\rm H\,I} = 2 \times 10^{20}$ cm^{-2}, $b = 40$ km s^{-1}, and $V_{\rm exp} = 100$ km s^{-1}, $F_{\rm red}/F_{\rm blue}$ reduces from $\sim$11 in the homogeneous case to $\sim$5 in the clumpy case. Since our homogeneous models consistently produce too large $F_{\rm red}/F_{\rm blue}$, this effect would certainly improve the overall fit of the expanding shell model spectra to our observed Lyα spectra.

While a highly inhomogeneous, multi-phase ISM is not fully consistent with LAE observations and may be astrophysically unrealistic (e.g., Scarlata et al. 2009; Duval et al. 2013; Laursen et al. 2013), several recent studies have shown that some degree of inhomogeneity is present for the average LAE (e.g., Blanc et al. 2011; Nakajima et al. 2012). These studies derive the parameter $q = \tau_{\rm Ly\alpha}/\tau_{1216}$, where $\tau_{\rm Ly\alpha}$ is the optical depth of Lyα photons and τ_{1216} is the optical depth of continuum photons redward of the Lyα transition. Values of $q \ll 1$ indicate that Lyα sees very little dust extinction, as would be the case for a reduced number of scatterings in an ISM that has either favorable kinematic properties (e.g., the gas experiences a high-velocity bulk motion, such as a powerful outflow), a highly inhomogeneous and clumpy distribution of neutral gas and dust (e.g., Neufeld 1991; Hansen & Oh 2006), or both. Values of $q \gg 1$ indicate that Lyα photons suffer a large number of scatterings and are thus strongly attenuated by dust, which is expected for a homogeneous and/or static ISM. For a sample of $\sim$900 LAEs at $z = 2.2$, Nakajima et al. (2012) calculated $\langle q \rangle = 0.7 \pm 0.1$, while Blanc et al. (2011) measure a median q of 0.99 ± 0.44 for LAEs in the HPS sample. Both of these measurements indicate that on average for a similar LAE to those we observe, Lyα photons are neither preferentially attenuated nor are preferentially escaping due to the configuration of the ISM. Although the effects of the ISM's distribution and kinematics both factor into the measured value of q, $q \approx 1$ indicates that some degree of ISM inhomogeneity cannot be ruled out.

In summary, the limitations of our Lyα radiative transfer modeling may be a factor in explaining some of the discrepancies between the model Lyα spectra and our observations. For HPS256, the expanding shell model properly reproduces the velocity offsets of the Lyα emission components. Including a distribution of frequencies for the input Lyα photons (which would create a broader emergent Lyα spectrum, better fitting the extended red wing of the red emission component) and modeling an inhomogeneous gas distribution within the expanding shell (which would decrease $F_{\rm red}/F_{\rm blue}$) would likely result in a model spectrum that closely matches our observations. However, such modeling advancements will not improve the fit when the velocity offsets of the Lyα emission components are not properly reproduced in the first place (e.g., the blue peak of HPS194 and HPS251).

5.2. Expanding Shells: The Right Model?

The expanding spherical shell model describing gaseous geometry and kinematics is appealing for star-forming galaxies due to its simplicity and physical motivation. This model has recently received a great deal of attention in the literature from an observational standpoint for interpreting Lyα line profiles of LAEs and LBGs and their velocity offsets. Verhamme et al. (2008) had success in fitting the Lyα line profiles of a sample of 11 LBGs (8 have EW$_{\rm Ly\alpha} > 20$ Å) observed at $R \approx 2000$ with expanding shell synthetic spectra. Their spectra were typically constrained by systemic redshift measurements of non-resonant emission lines in the low-resolution FORS Deep Field spectra of Noll et al. (2004). They use the physical parameters derived from those fits to explain several observed correlations between various properties of the sample. Of their 11 galaxies, 7 display an Lyα line with a single asymmetric peak. Their spectra are typically deep enough to detect the continuum, so secondary peaks are not missed due to S/N limitations. The remaining four galaxies show multiple-peaked morphologies similar to the Lyα spectra of the LAEs presented here. Unlike for the single-peaked asymmetric profiles, Verhamme et al. (2008) have difficulty fitting the double-peaked Lyα profiles with the expanding shell model and typically require quasi-static gas kinematics, much larger intrinsic Lyα line widths than are physical for non-AGN star-forming galaxies, or a large adjustment of the velocity zero point (of $\gtrsim$200 km s^{-1}) in order to obtain a good fit.

Observing LBGs with existing Lyα data at an average spectral resolution of $\sim$370 km s^{-1} FWHM, Kulas et al. (2012) specifically targeted objects displaying multiple-peaked Lyα spectra and followed up on a sample of 18 objects with NIR observations

of optical nebular emission lines to constrain the sample's z_{sys}. They observe various Lyα line profile morphologies and qualitatively compare composite spectra grouped by morphology with a coarse grid of synthetic spectra from the same expanding shell Lyα radiative transfer code used here. In general, they found that most features of the various multiple-peaked spectra could not be reproduced by the models. The best match to the expanding shell model is their "Group 1" profiles, which are qualitatively similar to the Lyα profiles in this work (see Figure 4). A high column density expanding shell model with $N_{\rm H\,I} = 2 \times 10^{20}$ cm^{-2}, $b = 40$ km s^{-1}, and $V_{\rm exp} = 100$ km s^{-1} reproduces the large velocity offsets for their composite "Group 1" LBG profile as well as the asymmetries. But, like we observe in Figure 7, the expanding shell model underpredicts the strength of their "Group 1" composite's blue emission component. Kulas et al. (2012) also measure the widths and velocity offsets of IS absorption features. Assuming that the absorbing material is part of the same outflowing shell through which Lyα photons scatter, the former measure traces b while the latter is equivalent to $V_{\rm exp}$. Indeed, they find qualitatively that the best-fitting model spectrum has $V_{\rm exp} = 100$ km s^{-1}, which is comparable to the 90 km s^{-1} blueshift of the "Group 1" IS absorption lines. However, their best-fit value of b is lower than that estimated from the observed IS absorption line widths for those objects by a factor of $\sim$7.

In addition to the aforementioned discrepancies between predicted Lyα line profiles from the expanding shell model and observed double-peaked Lyα profiles, the deep spectroscopy of faint LAEs from Rauch et al. (2008) has allowed for the study of spatial Lyα surface brightness (SB) profiles. The Rauch et al. (2008) sample is comprised of several single-peaked, asymmetric Lyα spectral line profiles as well as some that are double-peaked. Barnes & Haehnelt (2010) have predicted the SB profiles using radiative transfer models with various spatial and velocity configurations of the gas, including expanding shells. They find that Lyα radiative transfer through an expanding shell typically results in a flat spatial SB profile, which is at odds with the peaky composite profile of the faint LAEs in the Rauch et al. (2008) sample. While the faint LAEs of Rauch et al. (2008) may be in a different class of objects than the bright LAEs we observe, Rauch et al. (2011) have performed a similar comparison to Barnes & Haehnelt (2010) with the spatial Lyα SB profiles of single, bright LBGs having both single and double-peaked spectral line profile morphologies. In both cases, Rauch et al. (2011) determine that the flat spatial SB profile resulting from an expanding shell is inconsistent with the peaky Lyα SB profiles with extended wings that are observed. They conclude that better representations of the observed Lyα SB profiles for bright LAEs are found by modeling a point source of ionizing radiation within an optically thick, slowly expanding halo of neutral gas rather than a shell.

In this work, we have provided examples of LAEs whose double-peaked Lyα spectral line profiles are not well reproduced by radiative transfer through *homogeneous* expanding shells. The largest discrepancies are the flux ratio $F_{\rm red}/F_{\rm blue}$ and the velocity offset of the blue component. Extrapolating from Figure 5, one can decrease $F_{\rm red}/F_{\rm blue}$ *and* reduce the blue component velocity offset qualitatively in better agreement with the observed Lyα line profiles of these objects by decreasing the shell's $V_{\rm exp}$ well below 50 km s^{-1}, which is the smallest value in our grid. For this near-static case, the total velocity separation between the two emission components straddling the systemic Lyα line center are to first-order given by twice the value calculated using Equation (5). From Equation (5), it can be seen that reproducing the observed $\Delta v_{\rm tot}$ for essentially any value of b requires $N_{\rm H\,I} \sim 10^{-19}$ cm^{-2}, which is too low of a column density to simultaneously reproduce the large FWHM of each peak *and* the extended red wings in the observed Lyα data (see Figures 5 and 7). Additionally, the Hα derived star formation rates (SFR; uncorrected for dust; see Table 1) for these three galaxies are large for a typical LAE. Combined with their small sizes ($\lesssim$1.6 kpc; see Section 5.5) and dynamical masses (see Rhoads et al. 2013), the resulting SFR surface density $\Sigma_{\rm SFR}$ of these galaxies indicates that they should be driving strong outflows of $>$50 km s^{-1} if $V_{\rm exp}$ is comparable to the escape velocity (Heckman 2002; Newman et al. 2012). This strongly disfavors any quasi-static shell model.

Finally, to this point, we have ignored the second blue emission peak in the spectrum of HPS256 and HPS251 and assumed that these two galaxies represent typical double-peaked LAE. If this assumption is invalid and the second blue peak is Lyα emission from the same system, the expanding shell geometry can most likely be immediately ruled out as the geometric and kinematic configuration of the neutral gas distribution for these objects. Triple-peaked Lyα emission profiles can be produced by the expanding or infalling[14] shell geometry (cf. Figure 5), but not with the observed relative strengths of the various components when considering their respective locations relative to the velocity zero point.

5.3. Other Models

The aforementioned discrepancies between the expanding shell model and the observations should lead us toward considering different, or more complex gas geometries and velocity fields. These differences should include deviations away from spherical symmetry, unity covering factors, and strictly outflowing gas. Works such as Christensen et al. (2012) and Noterdaeme et al. (2012) incorporate multi-phase media in their gas geometries to closely reproduce multiple-peaked Lyα line profiles. The former work is actually an expanding shell (whose parameters are within the space covered by our grid: $N_{\rm H\,I} \approx 10^{18}$ cm^{-2}, $b \approx 90$ km s^{-1}, $V_{\rm exp} \approx 50$–100 km s^{-1}) that includes dense neutral clouds distributed within a more ionized and less dense "intercloud medium" inside the shell's cavity. The latter work incorporates an overall inflowing velocity field with starburst driven bipolar outflowing gaseous "jets" to account for the strong blueward Lyα emission they observe for a double-peaked line profile. A similar model was adopted by Adams et al. (2009) to constrain the spatially resolved 2D Lyα emission from a $z = 3.4$ radio galaxy, where ionized cones aligned with the galaxy's radio axis are embedded in an infalling neutral halo.

Current state-of-the-art modeling efforts are post-processing galaxy models drawn from hydrodynamic and cosmological galaxy formation simulations with Lyα radiative transfer codes (e.g., Zheng et al. 2010; Kollmeier et al. 2010; Barnes et al. 2011; Verhamme et al. 2012; Yajima et al. 2013). For example, Barnes et al. (2011) find that a typical halo contains a mixture of inflowing and outflowing gas and that the relative contribution of each along the line of sight determines the relative strength of the Lyα emission blueward (for inflow) and redward (for outflow) of the velocity zero point. As a result, the Lyα line

[14] The synthetic Lyα spectra produced by the shell geometry expanding at $V_{\rm exp}$ are also valid for a shell infalling with the same velocity, in which the Lyα profile is reversed about $\Delta v = 0$ km s^{-1} relative to the expanding case (Verhamme et al. 2006).

profile can vary as a function of viewing angle for the same halo. Also, Verhamme et al. (2012) post-processed high-resolution hydrodynamical simulations that follow the formation and evolution of isolated disk galaxies with an Lyα radiative transfer code. Their simulations resolve the small-scale structure of the ISM (including the thick, fragmented clouds in which stars form and the Lyα photons originate), which they find to be extremely important in determining the galaxy's Lyα properties. The clumpy disk galaxy they model harbors an axially asymmetric, large-scale outflowing velocity field that is mostly perpendicular to the disk. The asymmetric outflow aids in the escape of Lyα photons and results in galaxy inclination strongly affecting the observed Lyα emission in terms of the escape fraction and $EW_{Ly\alpha}$, the Lyα SB distribution, and the shape of the Lyα line profile. For edge-on orientations, they expect to observe more symmetric double-peaked Lyα spectra as a result of little-to-no outflow along the line of sight and the higher optical depth to the star-forming regions through the disk. For increasingly face-on orientations, increasing $EW_{Ly\alpha}$ and asymmetry between the two emission peaks should develop as the outflowing gas perpendicular to the disk gains a larger velocity component along the line of sight. While typical star-forming galaxies at $z \sim 2.4$ are likely not disks in the classical sense (e.g., Law et al. 2012a) and probably do not have bipolar outflows (e.g., Law et al. 2012b), the more realistic treatment of galactic systems by Verhamme et al. (2012) has shown the importance of considering Lyα radiative transfer on small scales within the ISM. Expanding shells modeling large-scale galactic outflows do not capture such physics, which may be an additional cause for the discrepancies we observe between the expanding shell model predictions and the spectrally resolved Lyα line profiles of the three LAEs.

5.4. Does $\Delta v_{Ly\alpha}$ Indicate the Magnitude of V_{exp}?

Many studies have used the results of Lyα radiative transfer through expanding shells to help explain the observed velocity offsets of the Lyα emission line from z_{sys} for star-forming galaxies and further to constrain the velocity of their large-scale outflows (e.g., McLinden et al. 2011; Finkelstein et al. 2011; Yang et al. 2011; Hashimoto et al. 2013; Guaita et al. 2013; M. Song et al. 2013, in preparation). The analysis in Section 4.3 of the spectrally resolved, multiple-peaked Lyα emission of the three LAEs we present shows that it is difficult to constrain some of the physical parameters of each galaxy's outflowing gas. This is especially true since even the best-fitting expanding shell radiative transfer models show major discrepancies when compared to the resolved Lyα spectra. Given these discrepancies, it is of note that $N_{H\,I}$ and b appear to be much better constrained than V_{exp}. For each galaxy, the best-fitting model has $N_{H\,I} = 10^{18}$ cm^{-2} and a high value of b as a result of their strikingly similar values of $\Delta v_{0,red}$ and $FWHM_{red}$. In addition, as can be seen in Figure 5, there is little change in the position of the dominant redward Lyα peak over the range $50 < V_{exp}$ (km s^{-1}) <200 for an expanding shell model with low neutral column density (i.e., $N_{H\,I} \lesssim 10^{20}$ cm^{-2}; see Section 4.2). Especially since this strong redward peak dominates the observed Lyα line profile at low spectral resolution and/or S/N, it appears that V_{exp} has the least influence on $\Delta v_{Ly\alpha}$ of the three physical parameters that we model for a galaxy with low neutral gas column density.

Several of the aforementioned studies (McLinden et al. 2011; Finkelstein et al. 2011; Guaita et al. 2013; M. Song et al. 2013, in preparation) do in fact utilize a lower spectral resolution that is similar to the HPS when observing Lyα such that objects with line profiles similar to those we present here are unresolved (see Figure 3). In cases for objects with multiple-peaked Lyα line profiles with Δv_{tot} less than the instrumental resolution, much of the information that is encoded in the multiple-peaked profile is lost and the only measurable quantity from the line profile becomes $z_{Ly\alpha}$ (or $\Delta v_{Ly\alpha}$ when a measure of z_{sys} exists). We have also previously noted the instrumental effect of observing an intrinsically asymmetric emission line at low resolution in which the peak flux can be biased in the direction of the extended emission tail (see Section 3.2.2). As a result of the loss of information, the measured $\Delta v_{Ly\alpha}$ for an unresolved line becomes a convoluted function of many parameters, including the line of sight velocity field, column density, and the temperature of the neutral gas in addition to parameters that were not explored in our models, such as dust content. Even when ignoring the possible effects of the IGM on the Lyα line profile (e.g., Dijkstra et al. 2006b; Laursen et al. 2011), the matter is further complicated when considering Lyα radiative transfer through more realistic models of the gas distribution and velocity fields for galaxies (see the previous subsection). These models, which do not have spherically symmetric gas distributions, indicate that viewing angle should also be an important parameter in determining the degree of flux asymmetry between the multiple peaks, which can affect the value of the measured $\Delta v_{Ly\alpha}$.

As a result of all of these factors, attempts to equate the velocity offsets from systemic that are observed in Lyα spectra to physical outflow speeds need to be treated with extreme caution. We also stress the importance of observing Lyα with high spectral resolution in order to extract the maximum amount of information from the line profile. We do point out, however, that while the *magnitude* of the inflow or outflow speed is not yet clearly a measurable quantity from the Lyα line profile even when spectrally resolved, the detection and sign of a non-zero $\Delta v_{Ly\alpha}$ does at least indicate presence of an outflow (neglecting IGM absorption) or potentially inflow (for blueshifted Lyα emission) along the line of sight.

5.5. Clues from Spatially Resolved Data

In Figure 8, we show CANDELS *HST* ACS/WFC F606W and WFC3/IR F160W images of the three LAEs, which probe the rest-frame UV (~1800 Å; this wavelength traces recent star formation through the continuum emission of young, massive stars) and rest-frame optical (~4700 Å), respectively. As expected from near-UV *HST* morphological studies of LAEs at similar redshift (e.g., Bond et al. 2012; Law et al. 2012b), the galaxies are compact with half-light radii[15] $r_e = 1.6$, 1.1, and 0.7 kpc for HPS194, HPS256, and HPS251, respectively, at ~2400 Å (Leauthaud et al. 2007).

At the spatial resolution of the *HST*, two of the galaxies (HPS194 and HPS251) are shown to have a companion continuum source at $\lesssim 1''$ distance.

HPS194. This galaxy consists of a compact source to the northwest with a possible tidal tail reaching toward the north (this is visible as small clumps in the rest-frame UV image and is a very pronounced continuous feature in the rest-frame optical image). A more diffuse companion is located ~0.″6 to the southwest in projection (~5 kpc if the sources are at the same redshift). As seen in Figure 1, the NIRSPEC slit used by Finkelstein et al. (2011) is aligned along the two sources. However, we were unable to detect Hα emission from the

[15] COSMOS ACS *I*-band Photometry Catalog, 2008 June Release.

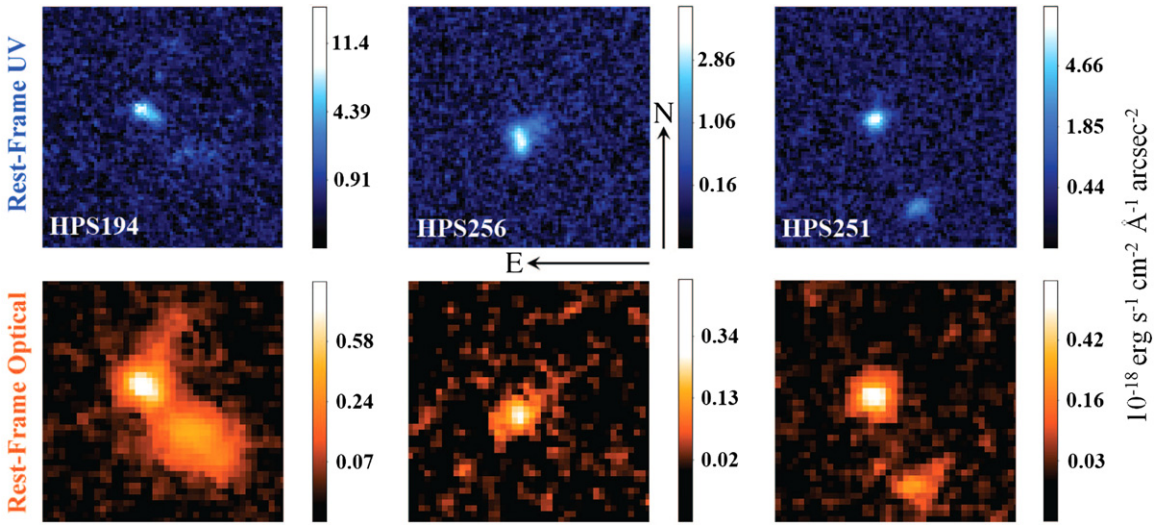

Figure 8. CANDELS *HST* images (Koekemoer et al. 2011) of the three LAEs, which show the stellar continuum morphologies of each galaxy. The top row shows ACS/WFC F606W images (which probe the rest-frame UV at ∼1800 Å) and the bottom row shows WFC3/IR F160W images (rest-frame optical at ∼4700 Å). Each panel is 2.″5 × 2.″5 (21 × 21 kpc at $z \sim 2.4$) in size, and their positions are indicated in the wider field Subaru *V*-band images shown in Figure 1 by the thick black boxes.

(A color version of this figure is available in the online journal.)

fainter source. As will be presented by G. A. Blanc et al. (2013, in preparation), we have also obtained deeper NIR spectra of HPS194 with the FIRE instrument (Simcoe et al. 2013) at the 6.5 m Magellan Baade telescope. A preliminary reduction of the data yields no detection of the diffuse companion's rest-frame optical emission lines. Although we cannot confirm from the available data if the compact and more diffuse sources lie at the same redshift, the disturbed, asymmetric morphology and possible tidal feature emanating from the northwest compact source is suggestive of an ongoing merger.

HPS251. This galaxy has a fainter, compact companion located ∼1.″0 (∼8 kpc) to the south–southwest in projection. Like HPS194, the NIRSPEC slit used by M. Song et al. (2013, in preparation) is aligned along the two sources. Unfortunately, two of the positions of the *ABBA* dither pattern positioned the dimmer source on the bottom edge of the slit, yielding insufficient S/N in the final 2D spectrum at the position of the companion. However, recent follow-up observations using FIRE have confirmed detections of [O III] λ4959 and [O III] λ5007 for both sources at the same redshift (these results will be presented by G. A. Blanc et al. 2013, in preparation). At the projected distance of ∼8 kpc, the two components of HPS251 are clearly interacting and will eventually merge.

While HPS256 does not have a companion within 1″, it does have several nearby continuum sources within ∼4″ to the southeast in projection (∼33 kpc if the sources are at the same redshift; see Figure 1). However, these sources are outside of the Mitchell Spectrograph's fiber and the NIRSPEC slit used by Finkelstein et al. (2011) was not aligned to include them.

Cooke et al. (2010) explored the Lyα properties of close LBG pairs and found that all showed Lyα in emission when the projected separation was $\lesssim$15 kpc. Their work supports the picture of galaxy–galaxy interactions triggering star formation and clearing gas and dust sufficiently for the Lyα photons produced in the starburst to escape the galaxies with high $EW_{Ly\alpha}$. Cooke et al. (2010) also find that while the 1D spectra of the close LBG pairs are often double peaked, they are resolved spatially into two distinct offset Lyα lines and corresponding continua in 2D spectra. For HPS194 and HPS251, this may be an alternative explanation for the multiple-peaked Lyα emission and why the expanding shell models poorly represent the data. However, our fiber-based Lyα spectra are spatially unresolved on the sky, so we cannot investigate potential spatial offsets of the spectrally resolved Lyα emission components for these galaxies with the current data. As seen in Figure 1, the potential companion sources for HPS256 and the confirmed companion to HPS251 are located outside of the Mitchell Spectrograph's fiber, even when considering the rms pointing uncertainty. Yet, we still observe the multiple-peaked Lyα line profile morphology. This makes it more likely that the multiple-peaked and asymmetric nature of the Lyα line for these galaxies is a consequence of radiative transfer effects in a non-static medium rather than being the result of the integrated Lyα emission from multiple sources at similar redshift.

Since all three galaxies have at least one nearby continuum source within a projected distance of $\lesssim$33 kpc and one of our galaxies has a *confirmed* companion within ∼8 kpc, a possible link between galaxy–galaxy interactions and luminous Lyα emission should not be ignored. This has recently been explored in the context of LABs by Yajima et al. (2013) who post-process hydrodynamical simulations of gas-rich binary major mergers with a 3D radiative transfer code. These authors find that such mergers produce copious Lyα emission (with Lyα luminosity $L_{Ly\alpha} \sim 10^{43}$–$10^{44}$ erg s^{-1}) that is extended over 20–50 kpc at $z \sim 3$ as a result of shocked gas and the starburst induced by the gravitational interaction. These properties are similar to typical $z \sim 3$ LABs (e.g., Matsuda et al. 2006). Due to the observational and selection methods utilized in the HPS (Adams et al. 2011), the $L_{Ly\alpha}$ observed for our three LAEs (∼10^{43} erg s^{-1}; see Table 1) is of the same order as that predicted by the Yajima et al. (2013) simulations. Additionally, the *total* velocity widths of the Lyα emission for HPS194, HPS256, and HPS251 are 667, 612, and 884 km s^{-1}, respectively (Adams et al. 2011), which are each comparable to the median value of 780 km s^{-1} for the LABs of Matsuda et al. (2006). However, since the Lyα spectra we present in this work supply no spatial information, we cannot currently assess the extended nature of the three LAEs individually. The HPS data are also of limited use in this

regard due to the coarse spatial resolution and limited depth of the survey (an upper limit of 7.″5 FWHM, which corresponds to the spatial resolution limit of the HPS, can be placed on each LAE's size; Adams et al. 2011). Future deep, spatially resolved Lyα spectra will be useful in determining if our LAEs are significantly extended, which would provide further evidence for the interaction scenario based on the simulations by Yajima et al. (2013).

Recently, Rhoads et al. (2013) used measurements of the SFR of bright LAEs (HPS194 and HPS256 were among the galaxies in their sample) along with measurements of their dynamical mass (which were assumed to be the upper limit of their gas mass) and sizes to compare such galaxies to existing star formation scaling relations. Daddi et al. (2010) established that there are two distinct sequences of star formation in the Kennicutt–Schmidt $\Sigma_{\rm SFR}$ versus gas mass density $\Sigma_{\rm gas}$ plane: a temporally extended sequence for "normal" star-forming disk galaxies, and a more rapid sequence for starburst galaxies that was determined from measurements of submillimeter and ultraluminous infrared galaxies (SMGs and ULIRGs, respectively). The latter scaling relation is offset above the former by 1.1 dex in the $\Sigma_{\rm SFR}$ versus $\Sigma_{\rm gas}$ plane. This bimodality between the star formation sequences of starburst and normal star-forming galaxies is largely due to the use of a bimodal conversion factor $\alpha_{\rm CO} = M_{\rm gas}/L_{\rm CO}$ used to convert the observed carbon monoxide line luminosity $L_{\rm CO}$ to gas mass $M_{\rm gas}$ ($\alpha_{\rm CO} = 4.6$ for normal star-forming galaxies and 0.8 for starburst galaxies). The measurements by Rhoads et al. (2013) suggest that LAEs lie above the scaling relation for normal star-forming galaxies and are consistent with the Daddi et al. (2010) starburst sequence at the $>3\sigma$ level. Thus, LAEs appear to form stars more rapidly than a typical star-forming galaxy at a given $\Sigma_{\rm gas}$. Note that the bimodality of $\alpha_{\rm CO}$ has recently been challenged by the simulations of Narayanan et al. (2012). These authors show that while $\alpha_{\rm CO}$ is systematically different for varying local galaxy conditions (e.g., metallicity and surface density), it varies smoothly among them. The result is a continuous, unimodal star formation scaling relation where the highest $\Sigma_{\rm SFR}$ disk galaxies overlap with the inferred mergers (i.e., starburst galaxies). The measurements for LAEs by Rhoads et al. (2013) show that LAEs occupy a region in the $\Sigma_{\rm SFR}$ versus $\Sigma_{\rm gas}$ plane bounded by $0 \lesssim \log \Sigma_{\rm SFR} \lesssim 1.3$ and $2 \lesssim \log \Sigma_{\rm gas} \lesssim 3.2$. Data points within this bounded area are consistent with the scatter in the continuous star formation scaling relation of Narayanan et al. (2012) and lie in a region of elevated SFR density occupied by both high-z disk galaxies and inferred mergers (i.e., low-z ULIRGs and high-z SMGs). Thus, the star formation observed for luminous LAEs is consistent with (but not necessarily suggestive of) that expected from an interacting or merging system.

In this scenario, interactions could be responsible for dispersing gas and dust and allowing Lyα photons to escape through low column density (i.e., low optical depth) "windows" in the overall neutral gas distribution. Combined with a low dust optical depth, the gravitationally induced burst of star formation could result in the large $\mathrm{EW}_{\rm Ly\alpha}$ we observe in addition to driving a strong large-scale outflow. Lyα radiative transfer through the dispersed (i.e., lower $N_{\rm H\,I}$) outflowing gas could give rise to the asymmetric, multiple-peaked Lyα line profiles with small Lyα velocity offsets, as compared to the Lyα spectra of LBGs that typically have large velocity offsets and smaller $\mathrm{EW}_{\rm Ly\alpha}$. Interaction-induced inflows of gas (resulting in star formation or shocks) along the line of sight could also help to enhance the Lyα flux blueward of the line center. Additionally, multiple blueward Lyα peaks (such as that observed for HPS256 and HPS251) could also be produced from shocked and/or fluorescing gas that is infalling along different sight lines. The large blueshift ($\sim$1000 km s^{-1}) of these Lyα peaks, however, likely indicates that such emitting material is not yet bound, unless radiative transfer effects couple favorably with the dynamics of the system to produce such large velocity offsets relative to the systemic velocity of the LAE's H II regions. To verify an interaction-based scenario for luminous LAEs, a larger sample of galaxies with confirmed redshifts for nearby companion continuum sources and spatially resolved Lyα spectra are needed.

The irregular nature of these galaxies' continuum morphologies and the confirmed and potential interactions with nearby companions may suggest that significant deviations away from Lyα point sources and spherical gas distributions and velocity fields are necessary for properly modeling Lyα radiative transfer through neutral gas on the galactic and circumgalactic scale. This conjecture is especially intriguing given that the two galaxies that are most poorly represented by the spherical expanding shell model Lyα spectra (i.e., HPS194 and HPS251) are the same two galaxies with the strongest evidence of an interaction.

6. SUMMARY AND CONCLUSION

In this paper, we have obtained follow-up optical spectra of three LAEs drawn from the HPS (Adams et al. 2011) with sufficient spectral resolution to resolve the Lyα emission line. With no preselection other than $F_{\rm Ly\alpha} > 10^{-16}$ erg s^{-1} cm^{-2} (which corresponds to $L_{\rm Ly\alpha} \gtrsim 10^{43}$ erg s^{-1} at $z \sim 2.4$), we find that all three galaxies at 120 km s^{-1} FWHM spectral resolution display multiple Lyα emission peaks. Using the NIR spectra of these galaxies' rest-frame optical emission lines from Finkelstein et al. (2011) and M. Song et al. (2013, in preparation), we have determined the velocity structure of the Lyα emission relative to the systemic redshift of each galaxy. Our main results are as follows.

1. The prominent double-peaks of the Lyα emission line for each LAE straddles and is asymmetric about the velocity zero point. The strongest emission peak is redshifted by 176 km s^{-1} on average relative to the systemic velocity and its velocity offset and basic shape are strikingly similar among the three galaxies in our sample. We observe larger variations from galaxy to galaxy in the emission blueward of the systemic velocity, including two of the three galaxies that display two separate weak blueshifted emission peaks. The most blueshifted of these weak peaks for these two galaxies is offset from the systemic redshift by $\sim$1000 km s^{-1}. However, the velocity offset of the redward peak and the peak-to-peak velocity separation between the two most prominent peaks that straddle the velocity zero point are $\sim 2\times$ smaller for each LAE than the same measurements made on average for Lyα-emitting LBGs with similar Lyα line profile morphologies. This is true even when taking into account the spectral resolution differences for each sample.
2. We have compared our Lyα spectra with the predicted line profiles of a grid of Lyα radiative transfer models in the popular and relatively idealized spherical expanding shell geometry to model large-scale galactic outflows. In contrast to the findings of works such as Verhamme et al. (2008) for single-peaked asymmetric Lyα line profiles, we observe several key discrepancies between the best-fitting models and the data. Visually, the redshifted Lyα

emission component is acceptably reproduced by models with low column density of neutral gas ($N_{\rm H\,I} = 10^{18}$ cm^{-2}). However, the blueshifted emission component ubiquitously has too little flux as compared to the data and has an incorrect velocity offset relative to the systemic velocity for two of the three galaxies (HPS194 and HPS251). Additionally, Lyα radiative transfer through an expanding shell cannot produce the highly blueshifted emission peak that is observed for HPS256 and HPS251.

3. Based on the above analysis, we caution against equating an observed velocity offset of Lyα directly with an outflow or inflow velocity, especially at low spectral resolutions where the Lyα line profile is unresolved and the intrinsic asymmetry of the emission line can bias the velocity offset measurement. The measured velocity offset, especially for unresolved Lyα spectra, is a complex function of many parameters describing the neutral gas, especially the column density $N_{\rm H\,I}$ due to its large dynamic range and ability to significantly change the width and asymmetry of the emission components. Additionally, the Lyα line profile shape and the resulting velocity offset can also be highly dependent on the viewing angle for more realistic, non-spherical gas geometries.
4. For luminous LAEs with $L_{{\rm Ly}\alpha} \gtrsim 10^{43}$ erg s^{-1}, like those in the HPS LAE sample, galaxy–galaxy interactions may play a significant role in producing and aiding the escape of copious Lyα photons and in shaping the emergent line profile by inducing star formation and clearing gas and dust. Such gravitational interactions may cause deviations away from spherical neutral gas geometries and velocity fields, such as those modeled in our expanding shell radiative transfer simulations. The effects of a non-spherical outflow in addition to simultaneous inflow of neutral gas, as well as smaller-scale Lyα radiative transfer effects within the ISM that are not captured in the expanding shell model could all contribute to the discrepancies we observe between the Lyα spectra of these galaxies and the predictions of the models.

In forthcoming work, we will extend this study to obtain spectrally resolved Lyα line profiles of a larger sample of $\sim$30 high EW$_{{\rm Ly}\alpha}$ LAEs using multi-object techniques. Of particular importance in the forthcoming work will be the ability to obtain at least one dimension of spatial information. The combination of a larger sample and >1D spectra will allow us to not only investigate the frequencies of various Lyα line profile morphologies among this unique sample, but also investigate the spatial distribution and possible extended nature of the Lyα emission. The latter may provide important constraints on the emission and escape mechanisms of Lyα photons from these systems.

T.S.C. acknowledges the support of a National Science Foundation Graduate Research Fellowship during this work. This research is partially supported by the National Science Foundation under grant AST-0926815 and the Texas Norman Hackerman Advanced Research Program under grant 003658-0295-2007. The construction of the Mitchell Spectrograph was possible thanks to the generous support of the Cynthia & George Mitchell Foundation. We thank McDonald Observatory and its staff for graciously supporting the observations. We additionally thank the following individuals for useful scientific discussions: V. Bromm, M. Fumagalli, J. Greene, D. Jaffe, J. Jardel, E. Komatsu, K. Kulas, E. McLinden, C. Scarlata, C. Steidel, V. Tilvi, and S. Tuttle. Finally, we acknowledge the anonymous referee for useful comments that have improved this paper.

REFERENCES

Acquaviva, V., Gawiser, E., & Guaita, L. 2011, ApJ, 737, 47
Adams, J. J., Blanc, G. A., Hill, G. J., et al. 2011, ApJS, 192, 5
Adams, J. J., Hill, G. J., & Macqueen, P. J. 2009, ApJ, 694, 314
Ahn, S., Lee, H., & Lee, H. M. 2000, JKAS, 33, 29
Barnes, L. A., & Haehnelt, M. G. 2010, MNRAS, 403, 870
Barnes, L. A., Haehnelt, M. G., Tescari, E., & Viel, M. 2011, MNRAS, 416, 1723
Becker, G. D., Hewett, P. C., Worseck, G., & Prochaska, J. X. 2013, MNRAS, 430, 2067
Berry, M., Gawiser, E., Guaita, L., et al. 2012, ApJ, 749, 4
Birnboim, Y., & Dekel, A. 2003, MNRAS, 345, 349
Blanc, G. A., Adams, J. J., Gebhardt, K., et al. 2011, ApJ, 736, 31
Bond, N. A., Gawiser, E., Guaita, L., et al. 2012, ApJ, 753, 95
Brammer, G. B., van Dokkum, P. G., Franx, M., et al. 2012, ApJS, 200, 13
Christensen, L., Laursen, P., Richard, J., et al. 2012, MNRAS, 427, 1973
Cooke, J., Berrier, J. C., Barton, E. J., Bullock, J. S., & Wolfe, A. M. 2010, MNRAS, 403, 1020
Cowie, L. L., & Hu, E. M. 1998, AJ, 115, 1319
Daddi, E., Elbaz, D., Walter, F., et al. 2010, ApJL, 714, L118
Dierckx, P. 1993, Curve and Surface Fitting with Splines (Oxford: Oxford Univ. Press)
Dijkstra, M., Haiman, Z., & Spaans, M. 2006a, ApJ, 649, 14
Dijkstra, M., Haiman, Z., & Spaans, M. 2006b, ApJ, 649, 37
Duval, F., Schaerer, D., Östlin, G., & Laursen, P. 2013, A&A, in press (arXiv:1302.7042)
Erb, D. K., Steidel, C. C., Shapley, A. E., et al. 2006, ApJ, 646, 107
Faucher-Giguére, C., Kereš, D., Dijkstra, M., Hernquist, L., & Zaldarriaga, M. 2010, ApJ, 725, 633
Finkelstein, S. L., Hill, G. J., Gebhardt, K., et al. 2011, ApJ, 729, 140
Finkelstein, S. L., Rhoads, J. E., Malhotra, S., & Grogin, N. 2009, ApJ, 691, 465
Finkelstein, S. L., Rhoads, J. E., Malhotra, S., Pirzkal, N., & Wang, J. 2007, ApJ, 660, 1023
Fynbo, J. P. U., Laursen, P., Ledoux, C., et al. 2010, MNRAS, 408, 2128
Gawiser, E., van Dokkum, P. G., Gronwall, C., et al. 2006, ApJL, 642, L13
Grogin, N. A., Kocevski, D. D., Faber, S. M., et al. 2011, ApJS, 197, 35
Gronwall, C., Bond, N. A., Ciardullo, R., et al. 2011, ApJ, 743, 9
Gronwall, C., Ciardullo, R., Hickey, T., et al. 2007, ApJ, 667, 79
Guaita, L., Francke, H., Gawiser, E., et al. 2013, A&A, 551, A93
Gunn, J. E., & Peterson, B. A. 1965, ApJ, 142, 1633
Haiman, Z., & Rees, M. J. 2001, ApJ, 556, 87
Hansen, M., & Oh, S. P. 2006, MNRAS, 367, 979
Hashimoto, T., Ouchi, M., Shimasaku, K., et al. 2013, ApJ, 765, 70
Heckman, T. M. 2002, in ASP Conf. Ser. 254, Extragalactic Gas at Low Redshift, ed. J. S. Mulchaey & J. T. Stocke (San Francisco, CA: ASP), 292
Heckman, T. M., Borthakur, S., Overzier, R., et al. 2011, ApJ, 730, 5
Hill, G. J., Gebhardt, K., Komatsu, E., et al. 2008a, in ASP Conf. Ser. 399, Panoramic Views of Galaxy Formation and Evolution, ed. T. Kodama, T. Yamada, & K. Aoki (San Francisco, CA: ASP), 115
Hill, G. J., MacQueen, P. J., Smith, M. P., et al. 2008b, Proc. SPIE, 7014, 701470
Hill, G. J., Tuttle, S. E., Lee, H., et al. 2012, Proc. SPIE, 8446, 84460N
Hu, E. M., & McMahon, R. G. 1996, Natur, 382, 231
Ilbert, O., Capak, P., Salvato, M., et al. 2009, ApJ, 690, 1236
Kelson, D. D. 2003, PASP, 115, 688
Kennicutt, R. C., Jr. 1998, ARA&A, 36, 189
Koekemoer, A. M., Faber, S. M., Ferguson, H. C., et al. 2011, ApJS, 197, 36
Kollmeier, J. A., Zheng, Z., Romeel, D., et al. 2010, ApJ, 708, 1048
Komatsu, E., Smith, K. M., Dunkley, J., et al. 2011, ApJS, 192, 18
Kornei, K. A., Shapley, A. E., Erb, D. K., et al. 2010, ApJ, 711, 693
Kulas, K. R., Shapley, A. E., Kollmeier, J. A., et al. 2012, ApJ, 745, 33
Kurucz, R. L., Furenlid, I., Brault, J., & Testerman, L. 1984, Solar Flux Atlas from 296 to 1300 nm (Sunspot, NM: National Solar Observatory)
Laursen, P., Duval, F., & Östlin, G. 2013, ApJ, 766, 124
Laursen, P., Sommer-Larsen, J., & Andersen, A. C. 2009, ApJ, 704, 1640
Laursen, P., Sommer-Larsen, J., & Razoumov, A. O. 2011, ApJ, 728, 52
Law, D. R., Steidel, C. C., Shapley, A. E., et al. 2012a, ApJ, 745, 85
Law, D. R., Steidel, C. C., Shapley, A. E., et al. 2012b, ApJ, 759, 29
Leauthaud, A., Massey, R., Kneib, J., et al. 2007, ApJS, 172, 219
Lee, J. 1974, ApJ, 192, 465
Mallery, R. P., Mobasher, B., Capak, P., et al. 2012, ApJ, 760, 128

Markwardt, C. B. 2009, in ASP Conf. Ser. 411, Astronomical Data Analysis Software and Systems XVIII, ed. D. Bohlender, P. Dowler, & D. Durand (San Francisco, CA: ASP), 251
Martin, C. L. 2005, ApJ, 621, 227
Matsuda, Y., Yamada, T., Hayashino, T., Yamauchi, R., & Nakamura, Y. 2006, ApJL, 640, L123
McLean, I. S., Becklin, E. E., Bendliksen, O., et al. 1998, Proc. SPIE, 3354, 566
McLinden, E. M., Finkelstein, S. L., Rhoads, J. E., et al. 2011, ApJ, 730, 136
Meeks, M. L. 1976, Astrophysics: Radio Observations, Methods of Experimental Physics, Vol. 12 C (New York: Academic)
Nakajima, K., Ouchi, M., Shimasaku, K., et al. 2012, ApJ, 745, 12
Nakajima, K., Ouchi, M., Shimasaku, K., et al. 2013, ApJ, 769, 3
Narayanan, D., Krumholz, M. R., Ostriker, E. C., & Hernquist, L. 2012, MNRAS, 421, 3127
Neufeld, D. A. 1990, ApJ, 350, 216
Neufeld, D. A. 1991, ApJL, 370, L85
Newman, S. F., Genzel, R., Förster-Schreiber, N. M., et al. 2012, ApJ, 761, 43
Noll, S., Mehlert, D., Appenzeller, I., et al. 2004, A&A, 418, 885
Noterdaeme, P., Laursen, P., Petitjean, P., et al. 2012, A&A, 540, 63
Oke, J. B., & Gunn, J. E. 1983, ApJ, 266, 713
Ono, Y., Ouchi, M., Mobasher, B., et al. 2012, ApJ, 744, 83
Ono, Y., Ouchi, M., Shimasaku, K., et al. 2010, MNRAS, 402, 1580
Ouchi, M., Shimasaku, K., Akiyama, M., et al. 2008, ApJS, 176, 301
Partridge, R. B., & Peebles, P. J. E. 1967, ApJ, 147, 868
Pentericci, L., Grazian, A., Fontana, A., et al. 2007, A&A, 471, 433
Pentericci, L., Grazian, A., Fontana, A., et al. 2009, A&A, 494, 553
Press, W. H., Teukolsky, S. A., Vetterling, W. T., & Flannery, B. P. 1992, Numerical Recipes in C: The Art of Scientific Computing (2nd ed.; Cambridge: Cambridge Univ. Press)
Rauch, M., Becker, G. D., Haehnelt, M. G., et al. 2011, MNRAS, 418, 1115
Rauch, M., Haehnelt, M. G., Bunker, A., et al. 2008, ApJ, 681, 856
Rhoads, J. E., Malhotra, S., Dey, A., et al. 2000, ApJL, 545, L85
Rhoads, J. E., Malhotra, S., Finkelstein, S. L., et al. 2013, ApJ, submitted (arXiv:1301.3140)
Scarlata, C., Colbert, J., Teplitz, H. I., et al. 2009, ApJL, 704, L98
Schaerer, D., Hayes, M., Verhamme, A., & Teyssier, R. 2011, A&A, 531, 12
Schaerer, D., & Verhamme, A. 2008, A&A, 480, 369
Scoville, N., Aussel, H., Brusa, M., et al. 2007, ApJS, 172, 1
Shapley, A. E., Steidel, C. C., Pettini, M., & Adelberger, K. L. 2003, ApJ, 588, 65
Simcoe, R. A., Burgasser, A. J., Schechter, P. L., et al. 2013, PASP, 125, 270
Song, M., Finkelstein, S. L., Gebhardt, K., Hill, G. J., & Drory, N. 2013, AAS Meeting Abstracts, 221, 147.36
Stark, D. P., Ellis, R. S., Chiu, K., Ouchi, M., & Bunker, A. 2010, MNRAS, 408, 1628
Steidel, C. C., Adelberger, K. L., Shapley, A. E., et al. 2000, ApJ, 532, 170
Steidel, C. C., Erb, D. K., Shapley, A. E., et al. 2010, ApJ, 717, 289
Steidel, C. C., Shapley, A. E., Pettini, M., et al. 2004, ApJ, 604, 534
Taniguchi, Y., Scoville, N., Murayama, T., et al. 2007, ApJS, 172, 9
Tapken, C., Appenzeller, I., Noll, S., et al. 2007, A&A, 467, 63
Tasitsiomi, A. 2006, ApJ, 645, 792
van Breukelen, C., Jarvis, M. J., & Venemans, B. P. 2005, MNRAS, 359, 895
Venemans, B. P., Röttgering, H. J. A., Miley, G. K., et al. 2005, A&A, 431, 793
Verhamme, A., Dubois, Y., Blaizot, J., et al. 2012, A&A, 546, 111
Verhamme, A., Schaerer, D., Atek, H., & Tapken, C. 2008, A&A, 491, 89
Verhamme, A., Schaerer, D., & Maselli, A. 2006, A&A, 460, 397
Willott, C. J., Chet, C., Bergeron, J., & Hutchings, J. B. 2011, AJ, 142, 186
Yajima, H., Li, Y., & Zhu, Q. 2013, ApJ, 773, 151
Yamada, T., Matsuda, Y., Kousai, K., et al. 2012, ApJ, 751, 29
Yang, Y., Zabludoff, A., Jahnke, K., et al. 2011, ApJ, 735, 87
Yuma, S., Ohta, K., Yabe, K., et al. 2010, ApJ, 720, 1016
Zheng, Z., Cen, R., Trac, H., & Miralda-Escudé, J. 2010, ApJ, 716, 574
Zheng, Z., & Miralda-Escudé, J. 2002, ApJ, 578, 33